

Conditions in the WR 140 wind-collision region revealed by the 1.083- μm He I line profile

Peredur M. Williams¹,^{*} Watson P. Varricatt,² André-Nicolas Chené,³ Michael F. Corcoran,^{4,5} Ted R. Gull,⁶ Kenji Hamaguchi,^{4,7} Anthony F. J. Moffat,⁸ Andrew M. T. Pollock,⁹ Noel D. Richardson,¹⁰ Christopher M. P. Russell,¹¹ Andreas A. C. Sander,¹² Ian R. Stevens¹³ and Gerd Weigelt¹⁴

¹*Institute for Astronomy, University of Edinburgh, Royal Observatory, Edinburgh EH9 3HJ, UK*

²*Institute for Astronomy, UKIRT Observatory, 640 North A'ohoku Place, Hilo, HI 96720, USA*

³*Gemini Observatory, Northern Operations Center, 670 North A'ohoku Place, Hilo, HI 96720, USA*

⁴*CRESST II and X-ray Astrophysics Laboratory, NASA/GSFC, Greenbelt, MD 20771, USA*

⁵*Department of Physics, Institute for Astrophysics and Computational Sciences, The Catholic University of America, Washington, DC 20064, USA*

⁶*Astrophysics Science Division, NASA/GSFC, Greenbelt, MD 20771, USA*

⁷*Department of Physics, University of Maryland, Baltimore County, 1000 Hilltop Circle, Baltimore, MD 21250, USA*

⁸*Département de physique and Centre de Recherche en Astrophysique du Québec (CRAQ), Université de Montréal, C.P. 6128, Succursale Centre-Ville, Montréal, QC H3C 3J7, Canada*

⁹*Department of Physics and Astronomy, University of Sheffield, Hounsfield Road, Sheffield S3 7RH, UK*

¹⁰*Department of Physics, Embry-Riddle Aeronautical University, Prescott, AZ 86301, USA*

¹¹*Department of Physics and Astronomy, University of Delaware, Newark, DE 19716, USA*

¹²*Armagh Observatory and Planetarium, College Hill, Armagh BT61 9DG, UK*

¹³*School of Physics and Astronomy, University of Birmingham, Edgbaston, Birmingham B15 2TT, UK*

¹⁴*Max Planck Institute for Radio Astronomy, Auf dem Hügel 69, D-53121 Bonn, Germany*

Accepted 2021 February 18. Received 2021 January 27; in original form 2020 November 30

ABSTRACT

We present spectroscopy of the P Cygni profile of the 1.083- μm He I line in the WC7+O5 colliding-wind binary (CWB) WR 140 (HD 193793), observed in 2008, before its periastron passage in 2009, and in 2016–2017, spanning the subsequent periastron passage. Both absorption and emission components showed strong variations. The variation of the absorption component as the O5 star was occulted by the wind-collision region (WCR) sets a tight constraint on its geometry. While the sightline to the O5 star traversed the WCR, the strength and breadth of the absorption component varied significantly on time-scales of days. An emission subpeak was observed on all our profiles. The variation of its radial velocity with orbital phase was shown to be consistent with formation in the WCR as it swung round the stars in their orbit. Modelling the profile gives a measure of the extent of the subpeak-forming region. In the phase range 0.93–0.99, the flux in the subpeak increased steadily, approximately inversely proportionally to the stellar separation, indicating that the shocked gas in the WCR where the line was formed was adiabatic. After periastron, the subpeak flux was anomalously strong and varied rapidly, suggesting formation in clumps downstream in the WCR. For most of the time, its flux exceeded the 2–10-keV X-ray emission, showing it to be a significant coolant of the shocked wind.

Key words: binaries: spectroscopic – circumstellar matter – stars: individual: WR 140 – stars: winds, outflows – stars: Wolf–Rayet.

1 INTRODUCTION

The collision of the hypersonic winds from the Wolf–Rayet (WR) and O stars in a massive binary system gives rise to a rich variety of phenomena observed from the radio to X-rays. Strong shocks are formed where the winds collide, leading to acceleration of particles, and heating and compression of the winds behind the shocks. The shock-compressed wind flows within the wind-collision region (WCR) and can sometimes be observed through the appearance of

orbital phase-dependent ‘subpeaks’ on emission lines and, in some cases involving WC-type stars, the formation of carbon dust.

The subject of this study is the WC7+O5¹ colliding-wind binary (CWB) system WR 140 (HD 193793), which has become an archetypal system on account of the strong variations in its radio, X-ray, and infrared (IR) emission – the last caused by episodic dust

¹Different spectral subtypes have been assigned over the years. The most complete classification is WC7pd + O5.5fc by Fahed et al. (2011), who employed spectral disentangling to classify the O star, but we use WC7 and O5 for brevity here.

* E-mail: pmw@roe.ac.uk

formation – all phase locked to its highly elliptical orbit (e.g. Williams et al. 1990). Variation of the profile of its 5696-Å C III emission line near the time of the 1993 periastron was first reported by Hervieux (1995). Around the following (2001) periastron, Marchenko et al. (2003) studied variations in the profiles of the C III and 5896-Å He I lines, while Varricatt, Williams & Ashok (2004) studied those of the 1.083-μm He I line. Previous spectroscopy of WR 140 by Vreux, Andriat & Biemont (1990), Eenens, Williams & Wade (1991), and Williams et al. (1992) had shown the 1.083-μm emission-line profile to have a flat top, characteristic of formation in the asymptotic region of the WR wind, with no evidence of a subpeak that could be formed in a WCR – but these observations happened to have been taken at orbital phases (0.56, 0.41, and 0.82, respectively) far from periastron passage. Nearer periastron, between phases 0.96 and 0.02, Varricatt et al. (2004) observed conspicuous subpeaks on the 1.083-μm line that, like those observed in the optical by Marchenko et al. (2003), shifted during orbital motion consistently with the changing orientation of the WCR and the flow of the emitting material along it. They also showed that the maximum radiative flux in the 1.083-μm He I subpeaks was greater than the 2–6 keV X-ray flux near the 1985 periastron or the 1–10 keV flux observed soon after the 1983 periastron, and was therefore a significant source of cooling of the shocked WC7 wind. Of course, the O5 stellar wind is also shocked in the WCR and we have to consider whether there is a contribution to the 1.083-μm subpeak from its helium. The O+O CWBs have yet to be surveyed for 1.083-μm subpeak emission, but the spectroscopic survey of the 1-μm region in OB stars by Conti & Howarth (1999) finds no 1.083-μm line emission in O5–O6 supergiants, including the CWB Cyg OB2 9 (Nazé et al. 2012) and the binary Cyg OB2 11 (Kobulnicky et al. 2012). Although we cannot rule out a contribution from the O5 wind in WR 140, these results suggest that the shocked O5 wind does not contribute to the subpeak emission, or the undisturbed O5 wind to the underlying emission profile.

Unlike the 5696-Å C III line, the profile of the 1.083-μm line in many WR stars also has a strong absorption component formed primarily in the asymptotic region of the stellar winds and valuable for measuring the terminal velocities (e.g. Eenens & Williams 1994). On the other hand, the O5 component is not expected to provide absorption in the 1.083-μm line, judging from the spectra of the O5f and O6f stars observed by Conti & Howarth (1999), or the O4V(f) star 9 Sgr observed by Varricatt et al. (2004), which do not show P Cygni profiles in their 1.083-μm lines. The contrast of the He I absorptions through the WC and O5 stellar winds can therefore provide a valuable tool for mapping the winds and WCR. The stars are too close together ($a = 9$ mas; Monnier et al. 2011) for us to resolve them with the spectroscopic instrumentation, so the observed profile is the superposition of the profiles formed in the separate, parallel sightlines to the O5 and WC7 stars. The 1.083-μm spectra of Varricatt et al. (2004) showed the absorption component to increase significantly between observations made before and after periastron passage as our lines of sight to the stars passed mostly through the O5 star wind in the first spectra and subsequently through the He-rich wind of the WC7 star in the later data. This allowed them to set constraints on the opening angle of the cone used to approximate the WCR, depending on the (then unknown) orbital inclination.

As part of the multiwavelength campaign to observe WR 140 around the time of the 2009 periastron, further observations of the 1.083-μm line profiles were made during 2008 from phase 0.93 to just before periastron. A strong subpeak was present on all spectra, while a sudden increase of the absorption component near phase 0.99 was used to estimate the opening angle of the WCR cone. A preliminary account of that work was given by Williams, Varricatt &

Adamson (2013) but we undertook two further observing campaigns in 2016–2017 to cover the following periastron passage in order to form a more complete picture of the evolution of the WCR at the most critical phases.

The principal scientific goals are to use the variation in 1.083-μm profile as the orbit progressed to map the WCR and to compare the flux emitted in the emission subpeaks on the 1.083-μm line, which occur over a wider range in phase than those on the optical lines, with the X-ray fluxes to study the cooling of the shocks. We had intended to compare the profiles of the 1.083-μm and 5696-Å subpeaks observed contemporaneously to see if they formed in the same or different regions of the WCR, but this was thwarted by poor observing weather at the critical phases. Although our observations cover less than one-seventh of the orbital period, they cover over 80 per cent of the orbit in terms of angular motion, so great is the eccentricity.

In this paper, Section 2 reports the collection of the data, and Section 3 presents the results: beginning with an overview of the variation of the line profiles, followed by discussion of the absorption and subpeak emission components. We discuss the results and relate them to studies at other wavelengths in Section 4 and summarize conclusions in Section 5.

2 OBSERVATIONS

The 2008 observations were made with the United Kingdom Infrared Telescope (UKIRT) on Mauna Kea, Hawaii, using the 1–5-μm UKIRT Imager Spectrometer (UIST; Ramsay Howat et al. 2004) in programme U/08B/17. The short- J grism and 4-pixel slit gave a resolution of 200 km s^{−1}. Observations generally comprised 12 integrations of 30 s, and spectra of the F5V star BS 7756 were observed at comparable airmass to WR 140 to correct for telluric absorption features, which are significant in this wavelength region. Wavelength calibration was performed using an argon lamp.

The first of our observations in 2016 were taken at phases close to conjunction (O5 star in front), also using UIST on UKIRT (programme U/16B/UA10). For these, the slit width was set to 2 pixels, giving a higher resolution of 100 km s^{−1}, and the A2V star BS 7769 was used as an additional telluric standard.

The spectra were not flux calibrated at the time of observation but flux calibration is provided via the continuum determined from the r and J photometry of the stellar wind. The level is taken to be constant during these observations because IR photometry, including observations in 2008, shows that the dust emission in the J band from the previous dust formation episode was no longer observable after phase 0.25 (Williams et al. 2009; Taranova & Shenavrin 2011). The stellar-wind continuum flux density at 1.08 μm, corrected for interstellar reddening, was found to be $F_\lambda = 4.33 \times 10^{-11}$ W m^{−2} μm^{−1}. A log of the UIST observations is given in Table 1, together with equivalent widths (EWs) of the absorption component and parameters of the emission subpeak to be discussed below. The phases were calculated using the ephemeris (Thomas et al. 2021) for periastron:

$$T_0(\text{MJD}) = 60636.23 + 2895.00E. \quad (1)$$

Further observations in 2016–2017 close to, and shortly after, periastron were made with Gemini North, also on Mauna Kea, using the Gemini Near-Infrared Spectrograph (GNIRS; Elias et al. 2006) in programmes 2016B-Q-49 and 2017A-Q-13. GNIRS was used in long-slit mode with the 110.5 line mm^{−1} grating in the sixth order (X band), short blue camera, and 2-pixel slit, giving a resolution of about 49 km s^{−1}, higher than those of the UIST spectra. Wavelength calibration was from an argon lamp. Each observation comprised eight integrations of 5 s, sometimes split over 2–3 co-adds. To correct

Table 1. Log of observations with UIST on UKIRT ordered by phase: those made in 2008 were taken using the 2-pixel slit and those in 2016 with the 4-pixel slit. Dates are in UT, quoted to 0.1 d. Also given are the equivalent widths (EWs) of the absorption component and the fluxes in the subpeaks, followed by their flux-weighted central velocities.

Date	Phase	Absorption EW (Å)	Subpeak flux ($10^{-14} \text{ W m}^{-2}$)	RVc (km s^{-1})
2008 June 27.6	0.9304	3.1 ± 0.2	2.5 ± 0.2	-1391 ± 102
2008 July 30.5	0.9417	2.4 ± 0.1	2.4 ± 0.1	-1431 ± 101
2008 August 5.4	0.9438	2.3 ± 0.1	2.8 ± 0.2	-1407 ± 102
2008 August 5.5	0.9438	2.2 ± 0.1	2.6 ± 0.2	-1413 ± 102
2008 August 22.4	0.9496	2.3 ± 0.1	2.7 ± 0.2	-1454 ± 104
2016 August 10.4	0.9555	2.3 ± 0.1	3.3 ± 0.3	-1462 ± 56
2016 August 25.3	0.9600	2.4 ± 0.1	4.0 ± 0.2	-1476 ± 55
2016 September 4.4	0.9634	2.3 ± 0.1	4.3 ± 0.2	-1455 ± 56
2016 September 19.4	0.9686	2.2 ± 0.1	4.6 ± 0.3	-1454 ± 58
2008 December 8.2	0.9869	2.9 ± 0.1	7.5 ± 0.2	-1080 ± 102
2008 December 19.2	0.9907	8.5 ± 0.1	8.5 ± 0.3	-697 ± 115
2008 December 20.2	0.9910	7.8 ± 0.1	8.9 ± 0.2	-712 ± 102
2008 December 21.2	0.9914	8.4 ± 0.1	8.7 ± 0.2	-645 ± 102
2008 December 22.2	0.9917	9.3 ± 0.1	8.2 ± 0.4	-639 ± 104
2008 December 23.2	0.9920	9.3 ± 0.1	8.6 ± 0.4	-613 ± 104
2008 December 24.2	0.9924	8.3 ± 0.1	9.0 ± 0.4	-563 ± 103

for telluric absorption lines, spectra of the A1V stars HIP 99893 or HIP 103108 were observed at comparable airmass. Besides the strong Paschen γ line at $1.0941 \mu\text{m}$, the A1V stars have significant C I lines at 1.0687 , 1.0694 , 1.0710 , and $1.0732 \mu\text{m}$ that were corrected for. Unfortunately, the HIP 103108 calibration spectrum on December 15 was observed in the wrong wavelength region and it was necessary to use a spectrum from another night and shift its wavelength scale to cancel, as far as possible, the telluric lines in the WR 140 spectrum. The GNIRS spectra were not flux calibrated at the time of observation and again our photometrically derived $1.08\text{-}\mu\text{m}$ continuum was used. For most of these observations it is necessary to allow for the additional contribution of dust emission to the continuum. This had the effect of diluting the line emission and absorption in our spectra. The additional flux was determined from the J -band photometry and assumed to be dust emission described by that of amorphous carbon grains at a temperature of 1100 K (Williams et al. 2009), allowing calculation of the $1.08\text{-}\mu\text{m}$ flux. From zero in the December 15 spectrum, the dust contribution at $1.08 \mu\text{m}$ grows to add 3.7 per cent of the stellar wind continuum by the December 27 observation, 7 per cent during the March–April series, and 6 per cent during the June observations. A log of the GNIRS observations is given in Table 2, where the EWs of the absorption components and the fluxes in the subpeaks have been adjusted to correct for the contribution by dust emission to the continuum. As an overview of the movement of the subpeaks, their flux-weighted mean radial velocities (RVs; as used by Fahed et al. 2011 for the $5696\text{-}\text{\AA}$ subpeaks) were measured and are also given in Tables 1 and 2.

3 RESULTS

3.1 Evolution of the line profile

A synoptic view of the evolution of the line profile is provided by the dynamic spectra presented in Fig. 1. The UKIRT/UIST and Gemini/GNIRS spectra conveniently fall into two sets separated by orbital phase and spectral resolution. The UKIRT/UIST (lower panel) spectra start at phase 0.9305, shortly before conjunction (O5 star in front, $\phi = 0.9554$), and continue to $\phi = 0.9925$, shortly

before periastron. Given in Table 3 for reference are the phases of the conjunctions and quadratures calculated using the values of orbital eccentricity, argument of periastron (O5 star), and inclination determined by Thomas et al. (2021): $e = 0.8993$, $\omega = 47^\circ 44'$, $i = 119^\circ 07'$. The profiles all show a subpeak on the broad emission component, initially apparently stationary at the ‘blue’ end (RV $\approx -1420 \text{ km s}^{-1}$) of the profile, and subsequently broadening and moving to longer wavelengths, it strengthened significantly between phases 0.9687 and 0.9867. We do not know the phase at which the subpeak first appeared; as noted above, it was not present in the profile Williams et al. (1992) observed at phase 0.83. The absorption component in our early spectra appears roughly constant before suddenly increasing sharply in the 11 d between phases 0.9869 and 0.9907. Thereafter, it remains strong and conspicuously variable in the approach to periastron (not reached in this sequence of observations as the source was setting), while the emission moves steadily to higher velocity.

The Gemini/GNIRS spectra (upper panel of Fig. 1) fall into three fairly concentrated sequences, in 2016 December, 2017 March–April, and 2017 June. The peak in the broad excess emission moved redward, especially between the first two spectra observed a week apart as the system went through periastron, and then continued moving redward to phase 0.0026 (December 27). Owing to their higher resolution (49 km s^{-1}), the GNIRS spectra resolve the absorption component better than the UIST ($100\text{--}200 \text{ km s}^{-1}$) spectra and, after phase 0.0324, show it to have a narrow core together with a variable, broad component. There is also a broad transient absorption feature near -1650 km s^{-1} in the 2017 June 17 spectrum ($\phi = 0.0621$) that had vanished by the following night. The broad emission subpeak continued its movement to higher velocities in the first five spectra, until 2016 December 27; thereafter, it was broader and weaker in the subsequent observations from 2017 March 23. The profiles are discussed below.

3.2 The absorption component of the $1.083\text{-}\mu\text{m}$ He I line profile

The EWs of the absorption components measured from our UIST and GNIRS spectra by direct integration are given in Tables 1 and 2. To

Table 2. Log of observations with GNIRS, giving equivalent widths (EWs) of the absorption component, fluxes, and flux-weighted central velocities. The absorption EWs and subpeak fluxes observed after periastron take account of the contribution of dust emission to the continuum as described in the text.

Date	Phase	Absorption EW (Å)	Subpeak flux (10^{-14} W m $^{-2}$)	RVc (km s $^{-1}$)
2016 December 15.2	0.9986	9.3 ± 0.3	22.3 ± 0.3	-148 ± 40
2016 December 22.2	0.0010	10.0 ± 0.2	22.6 ± 0.9	482 ± 84
2016 December 23.1	0.0013	10.4 ± 0.3	19.1 ± 0.4	710 ± 99
2016 December 24.0	0.0016	10.5 ± 0.2	18.6 ± 0.5	843 ± 30
2016 December 27.2	0.0028	10.6 ± 0.2	17.7 ± 0.5	950 ± 55
2017 March 23.6	0.0326	4.6 ± 0.2	18.5 ± 0.5	440 ± 30
2017 March 26.7	0.0337	7.2 ± 0.1	14.5 ± 0.4	416 ± 30
2017 March 27.7	0.0340	6.5 ± 0.1	9.0 ± 2.0	512 ± 30
2017 March 28.6	0.0343	7.2 ± 0.2	13.2 ± 0.6	389 ± 30
2017 March 30.6	0.0350	6.9 ± 0.2	15.2 ± 0.5	418 ± 30
2017 April 24.6	0.0437	6.4 ± 0.2	16.2 ± 0.6	333 ± 30
2017 June 17.6	0.0623	6.5 ± 0.1	10.3 ± 0.4	495 ± 30
2017 June 18.6	0.0626	6.7 ± 0.1	10.5 ± 0.5	308 ± 40
2017 June 19.6	0.0630	6.3 ± 0.1	6.4 ± 0.7	288 ± 60

ensure comparability of the results from the different instruments, the continuum for each measurement was determined by fits to the same wavelength regions, 1.069–1.071 and 1.104–1.108 μm , while errors were estimated from repeated measurements varying the choice of the ‘blue’ edge of the profile. The red edge of the profile is determined by the rising edge of the emission profile. A possible concern is that some emission from the subpeak when it is at its shortest wavelength could overlap with and fill in part of the absorption component, thereby weakening both features. We cannot rule out this possibility given the absence of undisturbed wind emission shortward of the subpeak. We note, however, that the absorption does not increase between the first and 10th spectra while the subpeak was moving to longer wavelengths, giving an increase of over 300 km s $^{-1}$ in RVc (Table 1; see also the profiles in Fig. 11 below) when it would be less likely to fill in the absorption, suggests that this is not a significant effect.

In addition, the absorption components and subpeak fluxes in the earlier UKIRT spectra observed by Varricatt et al. (2004), Eenens et al. (1991), and Williams et al. (1992) were remeasured using, as far as possible, the same methodology as for the new data, including correction for the contribution by heated dust to the 1.08- μm continuum at the times of the 2001 March observations. The EWs and subpeak fluxes from these observations are given in Table 4.

The EWs within $0.075P_{\text{orb}}$ of periastron are plotted against phase in Fig. 2. The highest EW is seen near conjunction, when the O5 star is furthest from us, but the most striking feature is the very sharp increase in the 11 d, 2008 December 8–19, prior to this maximum caused by the passage of the following arm of the WCR across our sightline to the O5 star, illustrated in Fig. 3. This increase must have begun at $\phi \simeq 0.986$, just before our December 8 observation, (cf. Table 1) and is modelled in Section 3.3 below.

As noted above, the observed absorption profile is the superposition of the profiles formed in the separate sightlines to the O5 and WC7 stars. That to the WC7 star always passes through at least part of the WC7 wind, that closest to that star, where the density is highest and most of the absorption occurs. Therefore, that component of the absorption is not expected to vary significantly round the orbit and we assume it to be constant. On the other hand, the extinction along the sightline to the O5 star through the WC7 wind varies systematically as the orientation and separation of the stars change with orbital motion and can be calculated given the orbit. If the cavity in the

WC7 wind blown by the O5 wind and WCR is large enough, and the orbital orientation favourable, the line of sight to the O5 star misses the WC7 wind for part of the orbit.²

This occurs around the time of conjunction when the O5 star and WCR are in front of the WC7 star, resulting in an interval ($0.94 < \phi < 0.97$) of low-absorption component EW. At these phases, the cavity blown in the WC7 stellar wind by the WCR is oriented towards us, so that the O5 star is observed through its own wind only that, as suggested by the spectra of luminous O4–O6 stars referred to above, is not expected to provide any extinction in the He I line. The extinction profile observed at these phases is then just that formed in the sightline to the WC7 star through its own wind, diluted by the unextinguished continuum of the O5 star. We can estimate the dilution by noting that Monnier et al. (2011) measured the WC7 star to be $1.37\times$ brighter than the O5 star in the *H* band and comparing the continuum spectral energy distributions (SEDs) of WC7 and O star models in the 1.06–1.65- μm range. This yields a flux ratio near 1.02 (WC7/O5)³ in the region of the He I line. Accordingly, we expect the EW of the absorption in the WC7-only profile to be around twice the EW observed around conjunction, i.e. 4.6 Å. This absorption will be present at all phases, together with that to the O5 star.

The variation of EW with phase shows significant scatter, greater than the observational uncertainties, on top of the expected smooth, orbitally dependent variation as the O5 star moves behind the WCR and into the denser WC7 wind. First, we consider the orbitally dependent variation, then the origin of the scatter.

3.3 Modelling the occultation of the O5 star

The rise to maximum absorption (Fig. 2) appears to occur in two stages, first the sharp rise at $\phi \simeq 0.986$ and secondly the rise through

²Because of the orbital motion, the WCR wraps around the stars in a spiral and the sightlines may pass through wind of the WC7 star several times; but as the wind density in the outer turns is much lower, the extinction in only the first turn of the spiral will be considered here.

³Extending this model to the visible, the flux ratio falls to 1.0, which compares with the range (1.37–0.5) found by Fahed et al. (2011) from dilution of the spectral lines in one or other of the components compared with single stars of similar types.

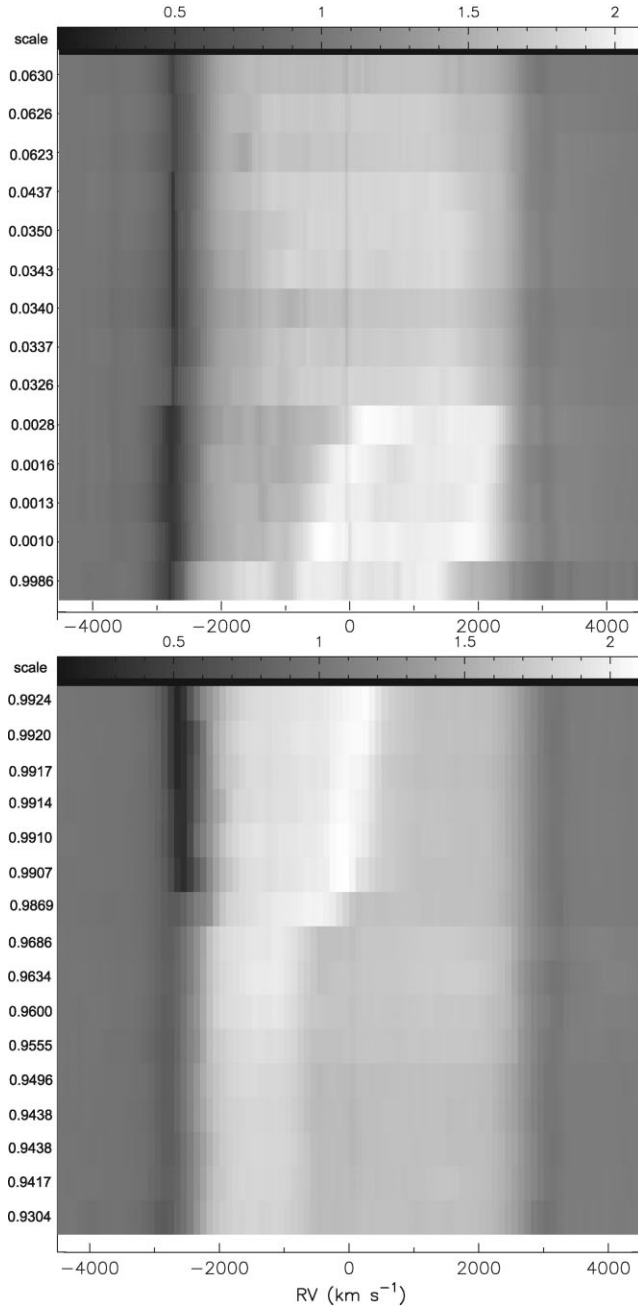


Figure 1. Dynamic spectra of the 1.083- μm profile before and after periastron, sequenced by orbital phase starting from $\phi = 0.93$ reading upwards, top panel from Gemini/GNIRS and lower panel from UKIRT/UIST. Flux scales are given on top of each panel. The data are not evenly spaced in phase and some abrupt changes reflect gaps in the coverage as can be seen from the labels on the y-axis. As described in the text, the spectra were observed at different resolutions.

Table 3. Benchmark phases in the orbit and that of the beginning of the sharp rise in absorption discussed below.

Phase	Phenomenon
0.0030	Conjunction, O5 star behind
0.0360	First quadrature
0.9554	Conjunction, O5 star in front
0.9966	Second quadrature
0.986	Beginning of sharp rise in absorption.

Table 4. Equivalent widths (EWs) of the absorption component and subpeak fluxes in 2000–2001 remeasured from the higher resolution ($R = 4700$) Cooled Grating Spectrometer 4 (CGS4) spectra observed by Varricatt et al. (2004), together with those from their UIST spectrum of 2003 and from the earlier Cooled Grating Spectrometer 2 (CGS2) and CGS4 spectra observed by Eenens & Williams (1994) and Williams et al. (1992). The EWs observed in 2001 also take account the contribution of dust emission to the continuum.

Date	Phase	Absorption EW (\AA)	Subpeak flux ($10^{-14} \text{ W m}^{-2}$)	Inst.
2000 Oct 13	0.9583	3.0 ± 0.1	3.3 ± 0.3	CGS4
2000 Dec 25	0.9835	2.6 ± 0.2	8.4 ± 0.3	CGS4
2000 Dec 26	0.9838	3.2 ± 0.2	8.4 ± 0.3	CGS4
2001 Mar 18	0.0123	6.8 ± 0.3	13.1 ± 0.5	CGS4
2001 Mar 31	0.0168	6.5 ± 0.2	13.2 ± 0.5	CGS4
2003 May 24	0.2876	5.2 ± 0.1	0.0	UIST
1988 June 28	0.408	4.5 ± 0.2	0.0	CGS2
1991 Oct 20	0.826	3.0 ± 0.3	0.0	CGS4

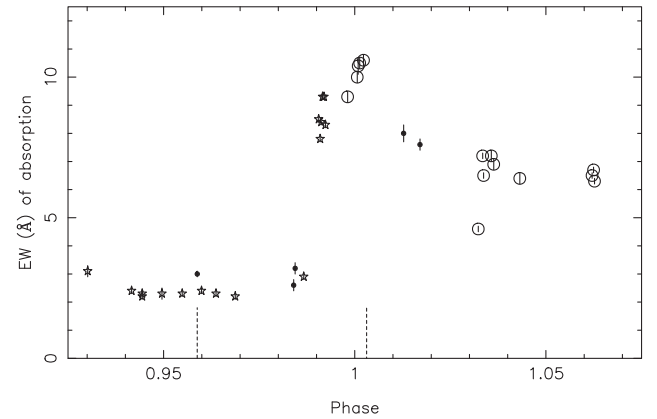


Figure 2. Equivalent width (EW) of the absorption component from the UIST (\star), GNIRS (\circ), and Varricatt et al. (2004) (\bullet) plotted against phase. The error bars are $\pm 1\sigma$. Vertical broken lines mark conjunctions, the O5 star in front near phase 0.96 and the WC7 star in front just after periastron. The phases of the conjunctions are given in Table 3.

periastron. Unfortunately, this result comes from two different cycles (2008 and 2016) and there is a gap in phase coverage, but we note a similar effect in the hardness ratio of the *Ross X-Ray Timing Explorer* (RXTE) Proportional Counter Array (PCA) data (Pollock et al., in preparation, Fig. 7), which also shows a pause in its increase near $\phi \simeq 0.995$, close to second quadrature on the way to maximum just after conjunction. The similarity of the X-ray and 1.083- μm absorption variations, despite the fact that the X-ray source is not coincident with the O5 star but lies in the WCR presumably close to the shock apex, suggests that the second stage of the rise to maximum is caused by the movement of the O5 star and the X-ray source further into and behind the WC7 stellar wind.

The 119° orbital inclination prevents the O5 star from being eclipsed by the WC7 star, but there is a significant decrease in impact parameter, p , between our line of sight to the O5 star and the WC7 star. It is given by

$$p = D \sin \psi, \quad (2)$$

where D is the separation of the stars and ψ is the angle between our line of sight and the line of centres between the WC7 and O5 stars. This angle is found from

$$\cos(\psi) = -\sin(i) \sin(f + \omega), \quad (3)$$

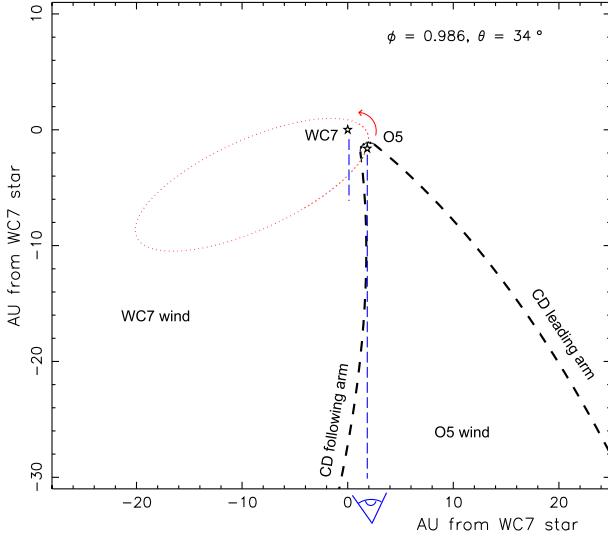


Figure 3. Sketch of the WC7 and O5 stars and the WCR configuration projected on to the plane of the observer at phase 0.986 showing the beginning of the occultation of the line of sight to the O5 star as it was intersected by the following arm contact discontinuity (CD, heavy dashed line) moving counterclockwise with the O5 star in its orbit (red) in this representation. The curvature of the CD and WCR is a consequence of the orbital motion and the radial flow of the winds, and varies round the orbit as the transverse velocity varies. (The sightline to the WC7 star was crossed earlier but this was not expected to affect the extinction, most of which occurs closer to the WC7 star where its wind is densest.)

where f is the phase-dependent true anomaly and i and ω are the orbital inclination and argument of periastron from Thomas et al. (2021) quoted above. The impact parameter falls from $p = 0.118a$ at second quadrature to $p = 0.059a$ at conjunction, where a is the length of the semimajor axis. Consequently, the sightline experiences significantly greater WC7 wind density and absorption between these phases. The increase in the extinction in the WC7 wind can be calculated using the relation for the X-ray extinction through a stellar wind as a function of orbit by Williams et al. (1990, appendix):

$$\tau \propto \frac{\sec i}{r \cos(f + \omega) \sqrt{\Delta}} \left[\arctan \left(\frac{-\sqrt{\Delta}}{\tan(f + \omega) \tan i} \right) \right], \quad (4)$$

where

$$\Delta = 1 + \tan^2(f + \omega) + \tan^2 i, \quad (5)$$

r is the distance from the intersection to the WC7 star, and f , ω , and i are as above. The extinction increases by a factor of 3.3 between these phases, but the influence on the observable EW of the He I line is much smaller because of the presence of the extinction towards the WC7 star itself.

The first stage of increase in extinction that near $\phi = 0.986$ is then interpreted as the passage of the edge of the WCR and WC7 wind across the sightline to the O5 star (Fig. 3), which we now model. The WCR straddles the surface where the stellar wind momenta balance, the ‘contact discontinuity’ (CD). Sufficiently far from the stars, and in the absence of orbital motion, the CD can be approximated by a cone (e.g. Girard & Willson 1987; Eichler & Usov 1993), having a half-angle, θ , which is determined by the properties of the colliding stellar winds, particularly the ratio of their momenta:

$$\eta = \frac{(\dot{M} v_\infty)_{\text{O5}}}{(\dot{M} v_\infty)_{\text{WC7}}}. \quad (6)$$

The relation between θ and η has been studied for different conditions in the shocked material, including purely radiative and adiabatic shocks by e.g. Gayley (2009). In this study, we will use the observations of the occultation near phase 0.99 to measure the angle θ directly and then consider η .

To derive θ from the observations, we have to take account of two further effects, the inclination of the orbit and the twisting of the cone by the orbital motion of the stars (Fig. 3). Seen from a non-zero inclination, the apparent opening angle of the cone will vary round the orbit, being equal to θ at quadratures only and smaller for most of the time, being reduced to zero if θ and the inclination are small enough. Writing θ' for the half-opening angle projected on to the observer’s plane through the apex of the cone, it is related to θ by

$$\cos \theta' = \frac{\cos \theta}{\sin(\arccos(\cos i \sin(f + \omega)))}, \quad (7)$$

where i , f , and ω are as above. To model the twisting of the WCR by orbital motion, we require the recent history of the transverse velocity, v_t , of the O5 star in its orbit in the WC7 wind calculated from the orbital elements, and the expansion velocity, taken to be the terminal velocity (2860 km s^{-1} ; Williams & Eenens 1989) of the WC7 wind, which dominates the structure on account of its greater momentum (cf. the consideration of the WR 104 pinwheel by Tuthill et al. 2008). An alternative position, which the expansion velocity is that of the slower wind (Parkin & Pittard 2008), also points to the WC7 star because its terminal velocity is lower than that (3100 km s^{-1} ; Setia Gunawan et al. 2001) of the O5 star. The shapes of the leading and following arms of the CD in the observer’s plane were calculated assuming the material to move ballistically at angles θ' and $-\theta'$ from the projected WC7–O5 axis, starting from the leading and following edges of the ‘rim’ dividing the ‘shock cap’ (Parkin & Pittard 2008), the curved region of the CD between the stars, from the cone beyond the O5 star. The rim is perpendicular to the WC7–O5 axis and its radius was taken⁴ to be $2r_{\text{O5}}$, where r_{O5} is the distance from the O5 star to the stagnation point of the WCR and is related to the separation of the stars, D , by

$$r_{\text{O5}} = \frac{\sqrt{\eta}}{1 + \sqrt{\eta}} D. \quad (8)$$

For each of a range of values of θ , the system configuration and CD were mapped for a sequence of orbital phases covering the observations. Because v_t varies significantly around the orbit, so does the curvature of the CD, which depends on the recent history of v_t .

At each phase, the intersection of the line of sight to the O5 star with the boundaries, the ‘leading’ and ‘following’ arms (see Fig. 3), of the CD was located and the distances to the WC7 star and absorption through its wind calculated. When the following arm of the CD crosses the sightline, it does so twice because of its curvature. As soon as it does so, the length of sightline passing through the WC7 wind increases rapidly as the orbit progresses. At the same time, the density of the WC7 wind traversed by the sightline increases as the stars approach each other. These effects combine to provide the rapid increase of absorption in a very short phase interval. The extinction in the WC7 wind to each of the intersection points was calculated using equation (4) above.

⁴The thin-shell models of Cantó, Raga & Wilkin (1996) give values in the range 2.0–2.2 for this factor, whereas Eichler & Usov (1993) give $\pi/2$. The exact choice within this range was found to make no difference to our modelling.

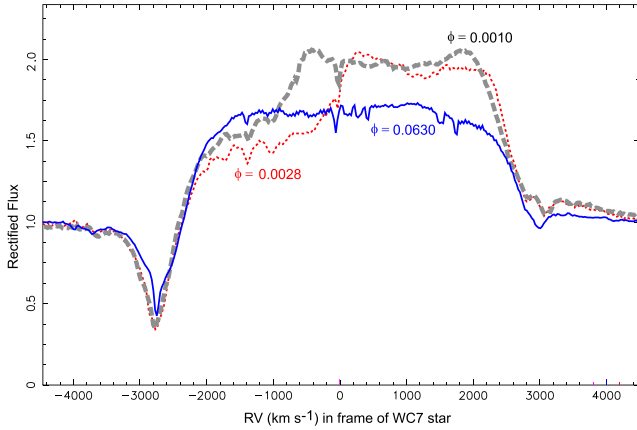


Figure 5. Comparison of line profiles observed with GNIRS superimposed to show development of broad absorption near periastron, $\phi = 0.0010$, and near conjunction, $\phi = 0.0028$ (dotted line, red), where the absorption extended from negative velocities to $\sim -1000 \text{ km s}^{-1}$ and zero (respectively), eroding the emission profile. For comparison, we show the spectrum observed on June 19, $\phi = 0.0630$ (blue), where the broad absorption has gone and the subpeak emission at its weakest. (The differences near $+3000 \text{ km s}^{-1}$ are not considered real but reflect imperfections in the correction for telluric features in the region of the Paschen γ line in the standard stars.)

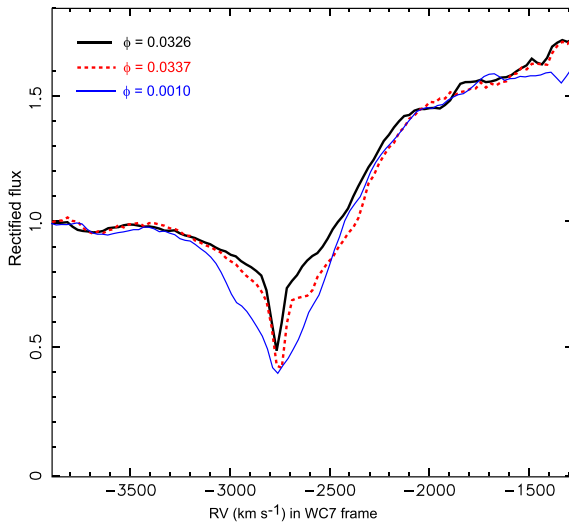


Figure 6. Comparison of absorption line profiles observed with GNIRS – all at the same instrumental resolution – showing development of broad absorption attributable to turbulence in the WCR instabilities in the first two of the 2017 March sequence of observations ($\phi \simeq 0.03$), and the even greater absorption observed on 2016 December 22 ($\phi = 0.0010$), very close to periastron.

consistent with the superposition of the $4.6\text{-}\text{\AA}$ absorption towards the WC7 star (see above) and about 4.6 \AA towards the O5 star through the WC7 wind. Three days later, the absorption is not only stronger but also the profile has wider wings, extending from ~ -3000 to -2400 km s^{-1} . The greater velocity range on its own might indicate thermal broadening, but the short-term variation points to formation in highly turbulent dense clumps. The sequence of observations (Table 2) from the next few nights shows variable absorption at a comparable level, indicating the presence of dense structures. What is puzzling, however, is that the broader absorption profiles are centred close to the terminal velocity of the WC7 wind. If turbulence was

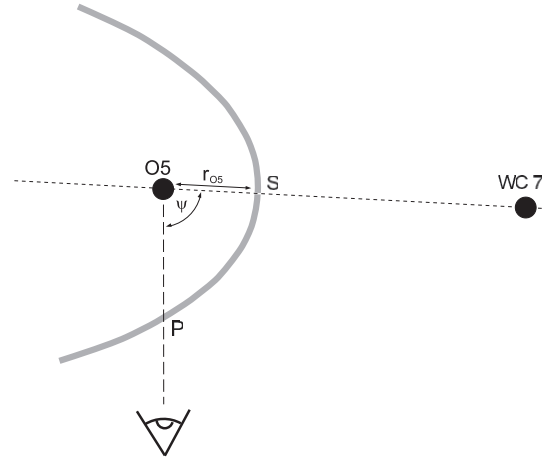


Figure 7. Sketch of the configuration at the time of the 2017 March sequence of observations ($\phi \simeq 0.03$). The positions of the WC7 and O5 stars and the WCR stagnation point (S) between them are marked. A thicker line shows the projection of the CD, which, in the absence of rotation, has cylindrical symmetry about the O5–WC7 axis. Our sightline to the O5 star crosses the CD at P. To show the relevant points, the sketch is not to scale.

isotropic, we might expect to observe velocities centred on that of the shock-compressed wind flowing along the CD where it is intersected by our pencil-beam sightline to the O5 star. The configuration at the time of the 2017 March observations is sketched in Fig. 7. The speed of the compressed wind along the CD at the intersection (P) with our sightline calculated from the O5 and WC7 wind velocities and the thin-shell model of Cantó et al. (1996) is $\sim 1600 \text{ km s}^{-1}$, giving an RV $\sim -1130 \text{ km s}^{-1}$. This is far from the centre of the observed broadening. The difference is even greater at the time of the $\phi = 0.0010$ observation (Fig. 6) immediately after periastron, which shows even broader absorption. At this phase, the angle between the line of centres and our sightline was smaller, $\psi = 39^\circ$, so that the intersection point P was closer to the stagnation point S and the speed of the compressed wind had reached only $\sim 770 \text{ km s}^{-1}$ at the intersection point and the component in our direction was only $\sim -260 \text{ km s}^{-1}$. The profile (Fig. 5) does show extension of absorption redward, only to $\sim -1000 \text{ km s}^{-1}$, which could be produced in the compressed wind flowing in the WCR. At $\phi = 0.0028$, $\psi = 29^\circ$ and the compressed wind is moving almost at right angles to our sightline, so its RV is $\sim -150 \text{ km s}^{-1}$. This is consistent with the broad absorption extending to near-zero RV observed in Fig. 5 but not with the central velocity of the strongest absorption component.

Inspection of the other GNIRS spectra shows that all of them are to some extent affected by broad absorption outside the narrow core seen in the 2017 March 23 spectrum (Fig. 6). The broader, variable absorption is taken to be that towards the O5 star during the phase range when our sightline to it passes through the WCR. Even the June sequence near phase 0.06, about 6 months after periastron, shows a transient broad absorption feature near -1650 km s^{-1} on June 17 (Fig. 1), which faded over the next two nights.

In contrast to the strong profile variations seen when our sightline passes through the WCR, the sequence of UIST observations in 2008 June to December ($0.92 < \phi < 0.98$), when we view the WC7 star through its own undisturbed wind, shows no evidence for short-term variation. This suggests that the observed line profile variations are caused by high-density regions or clumps in the WCR, while the undisturbed WC7 stellar wind is rather smooth and unclumped, at least far from periastron.

Near periastron, however, when the O5 star and WCR are beyond the WC7 star, the broadening of the high-velocity blueshifted P Cygni absorption component suggests some large-scale disturbance from the wind from the WC7 star, perhaps induced by the proximity of the O5 star. It is hard to envisage a mechanism for this effect – the wind of the O5 star is held close to that star by the WCR – but perhaps the combination of the O5 star’s continuum flux on the WC7 wind, coupled with the high orbital speed of the WC7 star near periastron, could somehow play a role.

The absorption components of the higher resolution (64 km s^{-1}) CGS4 spectra observed by Varricatt et al. (2004) in 2001 March are not significantly broader than those observed in 2000, suggesting that absorption by turbulent material in the WCR was not important at those times. This is in accord with the EWs, which show fading towards the sequence observed at a later phase in 2017 March (Fig. 2).

At this phase, we are sampling the WCR relatively close to the O5 star. To get an indication of the extent of the turbulence downwind along the WCR, we can use the first of the short-lived maxima listed in Section 3.2 above, the one while the absorption was rising in 2008 December. At this phase ($\phi \simeq 0.992$), the sightline cut through the WCR between 3 and 32 au from the O5 star, so that the clumps could be located anywhere in this range.

3.5 The emission components of the $1.083\text{-}\mu\text{m}$ He I line profile

The emission profile of the $1.083\text{-}\mu\text{m}$ line in WR stars is usually very broad owing to its formation where the wind has attained its terminal velocity, and often flat-topped owing to its low optical depth. In colliding wind binaries, the profile can be modified by two effects: the emission ‘subpeaks’ from the shock-compressed wind flowing in the WCR, and a possible deficit in the underlying profile owing to missing emission from the cavity in the WR wind caused by the WCR (Stevens & Howarth 1999) – provided that the WCR lies within the region of the WC wind where the $1.083\text{-}\mu\text{m}$ emission arises. To investigate this, we inspect the line formation calculated with an appropriate Potsdam Wolf–Rayet (PoWR) atmosphere model (e.g. Sander et al. 2015) for the WC7 star. While the detailed binary atmosphere analysis will be presented in a forthcoming paper, we found that most of the $1.083\text{-}\mu\text{m}$ line emission is generated within $100 R_*$. This is similar to what has been found for other WC wind models by Hillier (1989, WC5 star) and Dessart et al. (2000, WC8 star). More than 75 per cent of the line is formed within 1 au and 85 per cent within a distance corresponding to the separation of the WC7 and the O5 at periastron. Hence, we do not expect a strong effect on the emission line caused by a cavity in the WR wind and will assume an invariant underlying profile for the $1.083\text{-}\mu\text{m}$ emission line.

In order to characterize the emission subpeaks, we need a reference spectrum of the undisturbed WC7 wind. All the spectra in this programme were observed at phases at which the wind collisions were strong, and show at least some subpeak emission. The early observations made further from periastron showing flat-topped profiles referred to in Section 1 are unsuitable as subpeak-free templates for our spectra because they have lower resolution or poorer signal-to-noise ratio. Instead, a synthetic undisturbed wind spectrum was formed from the four (100 km s^{-1} resolution) UIST observations taken in 2016, taking their mean but replacing the fluxes in the velocity range -2100 to -500 km s^{-1} , covering the subpeaks, with the mean of the fluxes between -500 and $+500 \text{ km s}^{-1}$, omitting that at zero velocity that shows a dip from the photospheric absorption line in the O5 star. This is far from ideal, but the $1.083\text{-}\mu\text{m}$ subpeaks are, in

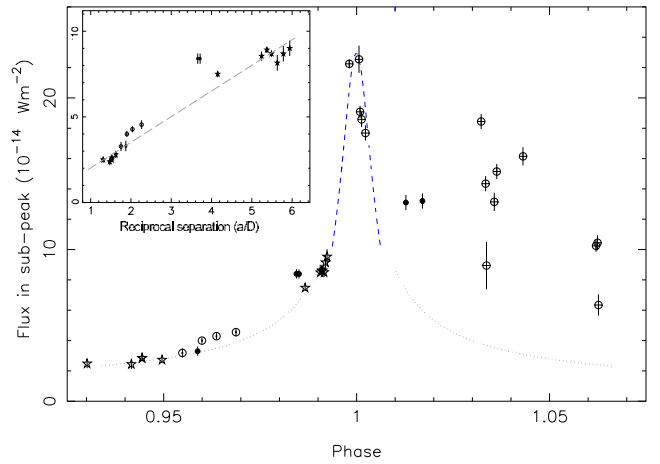


Figure 8. Flux in the emission subpeak from the UIST 2008 (★) and 2016 (⊙), CGS4 (●), and GNIRS (⊕) observations plotted against phase. Superimposed on the data is a dotted line representing the variation of the reciprocal of the separation of the WC7 and O5 stars, D , and a dashed line shows the variation of D^{-2} with phase, both with arbitrary normalization. The error bars are $\pm 1\sigma$. Inset: the $0.93 < \phi < 0.993$ fluxes plotted against reciprocal separation, a/D , of the stars.

most cases, so strong that such a template allows us to measure their fluxes and model their profiles without the introduction of significant uncertainties.

The fluxes in the subpeak were calculated by integrating the emission component, including all the features, subtracting the template spectrum, and converting to flux units using the continuum flux level derived above. They are listed in Tables 1 (UIST) and 2 (GNIRS).

The fluxes are plotted against orbital phase in Fig. 8. Prior to periastron, the subpeak fluxes increase steadily with phase, whereas, after periastron, they decline very irregularly. Up to $\phi \simeq 0.99$, the fluxes are approximately inversely proportional to the stellar separation, D , as can be seen in the plot against reciprocal separation, a/D , in the inset, suggesting that the shocked WC wind in the region of the WCR where the $1.083\text{-}\mu\text{m}$ subpeak arises is adiabatic in this phase range, by analogy with the expected $1/D$ variation of the X-ray luminosity with stellar separation in such a regime (Stevens et al. 1992) and in accord with their expectation that the shocks in WR 140 would be adiabatic for most of the orbit. Unfortunately, there is a gap in our temporal coverage because a spell of poor observing conditions prevented our getting intensive observations of the $1.083\text{-}\mu\text{m}$ subpeaks in the critical phase range, but it is apparent that, closer to periastron, the flux varied more steeply with separation than as D^{-1} , as can be seen by comparison with the dashed line in the figure. This chimes with the demonstration by Marchenko et al. (2003) and Fahed et al. (2011) that, between phases -0.01 and 0.01 , the flux in the subpeak on the $5696\text{-}\text{\AA}$ C III line varied with the separation approximately as D^{-2} . Taken together, these results suggest a change in conditions in the post-shock WC7 wind sometime near $\phi \simeq 0.99$, which may be related to the onset of dust formation at this phase⁵ and the requirement of efficient cooling for this to take place (Usov 1991).

⁵Dust emission first appears at $\phi = 0.0$ but there is some delay (Williams 1999) after the formation of sufficiently compressed wind for it to flow down the WCR to be far enough from the stars for the grains condensing in it to survive the stellar radiation fields.

Immediately after periastron, until $\phi \simeq 0.003$ when there is a gap in our coverage, the 1.083- μm subpeak flux appears to fade as D^{-2} but, later, when the observations resumed after $\phi \simeq 0.03$, it was found to fade very irregularly, sometimes on a short time-scale, with levels not far below the maximum near periastron. At this phase, the binary separation was the same as that at $\phi = 0.97$, so that the pre-shock densities of the undisturbed WC7 and O5 winds and therefore the wind material available to be compressed in the WCR would have been the same as those at the earlier phase. If the formation of the subpeak emission is by recombination, with emission proportional to the square of the density, formation in dense clumps, such as those found from the variations in the absorption component above, could be responsible given a suitably low filling factor and the clumps remaining optically thin in the line. Throughout our sequence of observations, up to $\phi \simeq 0.063$, the flux does not return to the levels and dependence on stellar separation seen before periastron. Further observations will be needed to determine at what phase it does so – and, indeed, the range in phase over which the subpeak is observable. For the present, we can divide the behaviour of the emission subpeak into three regimes. Prior to $\phi \sim 0.99$, the flux varied relatively smoothly proportionately to D^{-1} with the exception of two values near $\phi \simeq 0.984$ observed in 2000 (Table 4), which may reflect clumpiness or variation between cycles. Secondly, through periastron, the flux varied more steeply, possibly in proportion to D^{-2} , but the data are too sparse to be certain and further observations at higher cadence are needed to test this and check for short-term variations attributable to emission from clumps, such those seen in the later data. Third is the chaotic regime described above, where the post-shock wind appears to be very clumpy.

3.6 Modelling the 1.083- μm subpeak

The observational link between colliding winds and emission-line subpeaks comes from the systematic variation of their RV profiles as the orientation of the WCR and the shock-compressed wind flowing through it vary around the orbit (Lührs 1997). Provided that the winds collide at their terminal velocities, the shape of the WCR, which is determined by the wind-momentum ratio η , does not change, but other geometric parameters such as the orientation and twisting of the WCR from orbital motion, and the velocity of the compressed wind in which the subpeaks form, take up a range of values within the WCR – as does the line emissivity. These phenomena have yet to be comprehensively modelled, but geometric models for the systematic movement of the subpeaks in the spectra of CWBs during orbital motion were first developed by Lührs (1997) and since extended by Hill, Moffat & St-Louis (2002, 2018). Such models have the compressed wind moving at a constant ‘streaming velocity’, v_{strm} , in a shell near the surface of a cone approximating the WCR. Twisting of the WCR is accommodated by giving the cone a single tilt angle in the orbital plane. The subpeak-forming region is effectively collapsed to a ring on the cone where conditions, including (implicitly) the emissivity, are constant. Application of such a model, fitting the observed profiles as a function of phase, allows determination of quantities like θ , v_{strm} , the orbital inclination, i , the tilt angle, turbulence, and further parameters introduced to refine the model (Hill et al. 2018). Where the subpeaks are too weak for their profiles to be determined, the bulk RVs of the compressed wind can still be modelled in a similar way.

Fahed et al. (2011) applied the Lührs model to the variation of the 5696-Å subpeak velocities within $\sim 0.01P$ of the 2009 periastron, extending it to allow for the rapid variation of the tilt angle around periastron by introducing a constant phase shift, and deriving $\theta =$

$39^\circ \pm 3^\circ$, $v_{\text{strm}} = 2170 \pm 100 \text{ km s}^{-1}$, and $i = 55^\circ \pm 6^\circ$. Similar values to these were derived from the previous periastron passage by Marchenko et al. (2003).

In the case of the 1.083- μm subpeaks, we have observations of the line profile over a larger phase range, 0.93–0.07, which, because of the high eccentricity of the orbit, samples the geometry around most of the orbit, including both conjunctions and both quadratures. Because we already have values for quantities like the orbital inclination and θ from other observations, and can derive the flow velocity from the measured stellar wind velocities and η , we will not attempt to solve for them from the observed 1.083- μm subpeak velocities but will instead examine the extent to which the velocities can be recovered taking into account the effects that we believe may be determining them.

Earlier studies with smaller data sets by Varricatt et al. (2004) and Williams et al. (2013) modelled the 1.083- μm subpeak emission by considering it to arise on a cone, analogously to the Lührs model. Here the flow velocity was taken to be the asymptotic velocity of the compressed wind, v , calculated from the WC7 and O5 terminal wind velocities (Williams & Eenens 1989; Setia Gunawan et al. 2001) following the thin shell wind-collision model of Cantó et al. (1996, equation 29), which is based on the conservation of the momenta of the two stellar winds. Resolving its components v_{axis} parallel to and v_z perpendicular to the axis of symmetry, the emission by material flowing on this cone at any phase has RVs in the range

$$\text{RV} = v_{\text{axis}} \cos(\psi) \pm v_z \sin(\psi), \quad (9)$$

where ψ , the phase-dependent angle between our line of sight and the axis of symmetry of the WCR (equal, in the absence of orbital motion, to the line of centres through the WC7 and O5 stars), is defined in equation (3) above.

Varricatt et al. (2004) showed that such a model reproduced the variations of the RV and velocity width of the 1.083- μm subpeak in their small data set, for an opening angle $\theta = 60^\circ$ and inclination $i \simeq 65^\circ$. With addition of the 2008 UIST data, the velocity variations could be recovered by a similar model but with a smaller opening angle, $\theta = 50^\circ$ (Williams et al. 2013), while including our new 2016–2017 data, application of such a thin-shell model suggested $\theta = 53^\circ$.

These values of θ derived from the subpeak are significantly greater than that, $\theta = 34^\circ$, derived above from the eclipse of the WCR. This difference suggests that the subpeak emission formed some distance from the CD in the shocked WC7 wind in the adiabatic region of the WCR – at least in the phase range when the post-shock WC7 wind was adiabatic – analogous to formation in the centre of a thick mantle in the Lührs model.

We now explore the ways in which the modelling can be extended to gain insights into processes in the WCR when wind-collision effects are at their strongest, taking advantage of the range of orientations of the WCR system determined by the well-constrained orbit. We are not attempting to model the likely variation of the subpeak emissivity in different regions of the WCR but there are several physically motivated respects in which the simple geometric models can be developed.

First, we need to consider emission from that region of the WCR where the compressed wind is still accelerating to its asymptotic velocity reached ‘downstream’ in the region of the WCR that can be approximated by a cone. This follows from our observation of strongly varying absorption in the 1.083- μm profile when the sightline passes through the curved region of the WCR between the stars, the ‘shock cap’ (Parkin & Pittard 2008), so we must consider

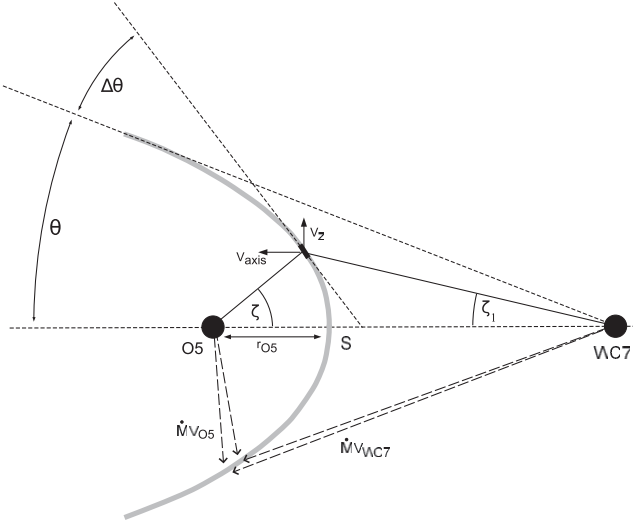


Figure 9. Sketch of the contact discontinuity (CD, grey) where the momenta, $\dot{M}v$, of the WC7 and O5 winds balance. It crosses the line of centres at the stagnation point (S) and has cylindrical symmetry about that line. Each point on it can be specified by the angles ζ and ζ_1 at the O5 and WC7 stars, respectively. In the asymptotic limit, ζ_1 corresponds to the opening angle θ . The subpeak emission is assumed to arise in a shell outside this in a region of angular width $\Delta\theta$ and the flow to originate on the CD between the asymptotic region and the tangent point corresponding to $\Delta\theta$.

emission arising there too. We do not have a generalized relation for the acceleration of the compressed wind from the stagnation point or a relation between its velocity and the angle between its direction and the axis of symmetry so will use the thin-shell model of Cantó et al. (1996). The condensed wind accelerates along the CD (Fig. 9, which follows Cantó et al. 1996 but replaces their θ and θ_1 with ζ and ζ_1 to avoid confusion with the opening angle θ), with velocity rising from zero near the stagnation point, S, to its asymptotic value when the angle ζ_1 at the WC7 star matches the WCR opening angle θ . This ties in the suggestion above that the subpeak emission arises in a shell of angular thickness $\Delta\theta$ on the WC7 side of the CD by considering the compressed wind to arise on the CD between the tangent point of the $\Delta\theta$ limit (Fig. 9) and the asymptotic value determined by θ . Depending on the extent along the WCR over which the emission forms, which can be specified in terms of the angle ζ at the O5 star, the compressed wind takes up a range of velocities and angles to the axis of symmetry instead of the single values used in previous modelling. We do not expect parcels of material arising from different regions of the CD to retain their initial velocities, which will give rise to Kelvin–Helmholtz instabilities, but expect the average bulk velocity of the compressed wind to be lower than its asymptotic velocity.

Secondly, near periastron, the CD may move close enough to the O5 star so that its wind has not reached terminal velocity that could cause the shock to weaken (Sugawara et al. 2015). If the radius of the O5 star is comparable to those of luminous O5 stars ($R_* \simeq 13$ – $18 R_\odot$; Repolust, Puls & Herrero 2004) and its wind accelerated according to the β -law, $v(r) = v_\infty(1 - R_*/r)^\beta$, with $\beta = 1$, the velocity at collision would be $\simeq 0.65v_\infty$ at periastron but closer to v_∞ for most of our observations. The shape of the WCR is unlikely to be affected because it depends on the balance of the wind momenta so that, by continuity, while the stellar wind is still accelerating, it will have a proportionately higher density than if it were moving at a constant rate, thereby preserving its momentum. The velocity of

the compressed wind, however, will be lower and vary with phase, which is included in the modelling.

Thirdly, orbital motion will cause the axis of symmetry of the WCR to lag behind the line of centres through the stars. The relative motion of the stars causes the axis of the WCR to lag by an ‘aberration’ angle determined by the ratio of the transverse velocity, v_t , calculated from the orbital motion, to the expansion velocity. In a long-period system like WR 140, this angle is generally small, reaching only 4.7° at periastron. Downstream of the O5 star, the axis of symmetry, and WCR are further twisted by the orbital motion, increasing with distance from the stars into a spiral structure. In this case, the degree of curvature depends on the recent history of the transverse velocity, v_t , of the O5 star, WCR in the orbit, and the expansion velocity, in the same way as the leading and trailing arms of the WCR modelled for the occultation in Section 3.3 above. Consequently, the downstream twisting effect is potentially greater than the aberration and strongest sometime after periastron. It was determined for each phase by calculating, as a function of downstream distance, the difference in phase and hence that in the angle ψ (equation 3) between the axis and our sightline. This was added to the aberration angle for calculation of the velocities.

Before modelling the subpeak profiles, we first examined the variation of the observed flux-weighted central RVs (Tables 1, 2, and 4) with phase and compared the variation with that modelled using $RV = v_{\text{axis}} \cos(\psi)$ (cf. equation 9). The opening angle, θ , was fixed at that determined above (Section 3.3) and the flow velocity was calculated for a series of incremental values of the width, $\delta\theta$, spaced by 1° up to the limit $\Delta\theta$ from the stellar wind velocities following Cantó et al. (1996, equation 29). To use this equation, it is necessary first to determine the position of the tangent point on the CD characterized by ζ and ζ_1 for a given angle $\delta\theta$, which can be found from

$$\tan(\theta + \delta\theta) = (\eta(\zeta - \sin\zeta \cos\zeta) + \zeta_1 - \sin\zeta_1 \cos\zeta_1) / (\eta \sin^2\zeta - \sin^2\zeta_1), \quad (10)$$

where ζ_1 , if small, is related (equation 26 of Cantó et al. 1996) to ζ by

$$\zeta_1 = \sqrt{15/2(-1 + \sqrt{1 + 0.8\eta(1 - \zeta/\tan\zeta)}), \quad (11)$$

and the wind-momentum ratio, η , was calculated from our opening angle $\theta = 34^\circ$.

This gives a series of flow velocities and angles, ζ , from which we derive a series of $v_{\text{axis}} = v \cos(\theta + \delta\theta)$. For the twisting, we determined for each phase a series of values of the angle ψ as a function of downstream extent. We used these and the axial flow velocities to derive the RVs. They are effectively volume-weighted but, in the absence of knowledge of the emissivity, we associated them with the flux-weighted RVs.

We used two fitting parameters, the angular thickness of the subpeak emitting region, $\Delta\theta$, and the downstream extent of the region twisted by the orbital motion. To allow for the varying size of the WCR around the orbit, we parametrized the latter by a constant multiple of the stellar separation, D , for simplicity; in practice, the emission is likely to fall off with distance from the stars as the density falls. The data and model velocities are compared in Fig. 10, from which we see that the variation of the central RV with phase is recovered around most of the orbit – including both conjunctions and both quadratures. We did not find it necessary to adopt different value of $\Delta\theta$ for different phase ranges and that it was fairly tightly constrained to $10^\circ \pm 5^\circ$. This width is consistent with that expected (20°) of the adiabatic WCR region corresponding to

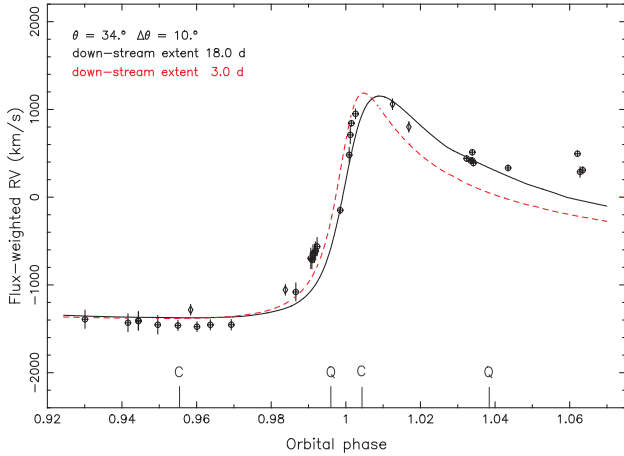


Figure 10. Measured flux-weighted central RVs (\oplus this study, \diamond RVs from spectra observed by Varricatt et al. 2004; error bars $\pm 1\sigma$) of subpeaks compared with those calculated (line) using the adopted orbital elements and phase-dependent velocity component v_{axis} calculated as in the text. Short vertical lines labelled ‘C’ or ‘Q’ mark the phases of conjunctions and quadratures.

our $\theta = 34^\circ$ (Ignace, Bessey & Price 2009; Pittard & Dawson 2018) and the formation of the subpeak within it. When the post-shock wind becomes radiative, the WCR is expected to become narrower, but we do not have enough data to test the effect of this on $\Delta\theta$.

The RV data were not well fit with a single value for the downstream emission extent over the whole phase range; it appears that the extent is much greater ($18D$) after periastron than in the $0.02P_{\text{orb}}$ before it, when an extent of $3D$ gives a better fit. As can be seen from Fig. 10, data at earlier phases do not allow us to discriminate because the transverse velocity and its recent history were very low. On the other hand, at phases shortly after periastron, when the transverse velocity had been at its maximum, the downstream twisting is greatest, its effect on the subpeak profile as modelled can provide a measure of the extent of the subpeak emission. As noted above, the subpeak fluxes are significantly stronger after periastron, possibly owing to their formation in dense clumps, so that the difference in downstream extent of the emission suggests that these clumps survive longer in the WCR than the compressed wind before periastron.

3.7 Modelling the subpeak profiles

We next sought to model the profile at the phases of our observations. The WCR was modelled as a series of annuli about an axis of symmetry, which deviates from the line of centres owing to the orbital motion as described above.

The RV from any element on the annulus can be considered as the sum of three components: V_1 , the projection of the flow parallel to the axis; V_2 , the projection of the flow perpendicular to the axis and also to the orbital plane; and V_3 , the projection of the flow perpendicular to the axis and within the orbital plane. They are given by

$$V_1 = v_{\text{axis}} \cos(\psi), \quad (12)$$

$$V_2 = v_z \sin(\chi) \cos(i), \text{ and} \quad (13)$$

$$V_3 = v_z \cos(\chi) \sin(i) \cos(f + \omega), \quad (14)$$

where χ is the azimuth along the annulus on the WCR, with $\chi = 0$ defined as being in the plane of the orbit on the leading edge of the

WCR, and the angle ψ , orbital parameters i, f, ω , and components of the compressed wind flow v_{axis} and v_z are all as above. The RV components V_2 and V_3 were calculated for a series of angles χ around each annulus.

The velocity components v_{axis} and v_z depend on the location of the annulus on the WCR, which we specify by the angle ζ (Fig. 9) determined from the region of the WCR specified by $\Delta\theta$ as above. For the velocity of the compressed wind at each point on the CD specified by ζ , we used Cantó et al.’s equation (29).

In addition, we need to consider possible lack of cylindrical symmetry in the emission from the annuli around the WCR axis, particularly between the leading and following arms of the WCR as a result of the orbital motion. Hydrodynamical modelling of adiabatic WCRs by Lamberts et al. (2012) shows that the outer shocks on the leading and following arms of the WCR can have different extents and densities. The effect on the observed subpeak emission will vary round the orbit. Near conjunctions, in the absence of orbital motion, the compressed wind flowing on the leading and following arms would have similar angles to our sightline and hence similar projected RVs, so that any such asymmetry in the WCR densities would not be observable. In contrast, the effects would be greatest near quadrature, when the projected flows on the leading and following arms have opposite signs.

Weighting of the emission for azimuthal asymmetry in the WCR can be modelled as a function of the azimuthal angle χ defined above by

$$wt(\chi) = (1 + A_1 \cos(\chi)) \times (1 - A_2 |\sin(\chi)|), \quad (15)$$

where the first term distributes emission between the leading and following arms and the second term distributes emission in or out of the orbital plane. A positive value of A_1 favours the leading arm and a positive value of A_2 favours the orbital plane (over regions above and below it), so that, for example, if A_1 and A_2 have equal positive values, the product of the two terms loads the leading arm of the WCR, tapering out of the plane, and keeping the same lower weight around the rest of the annulus.

The adjustable parameters defining any model are the width, $\Delta\theta$, of the emitting region, which gives the lower limit on ζ defining the range on the CD from which the subpeak is formed, the downstream extension of the emission for the twisting of the WCR, and the asymmetry parameters, A_1 and A_2 . The relative flux at each velocity in the range $\pm 4500 \text{ km s}^{-1}$ was calculated and the resulting profile was then convolved with Gaussian profiles for the turbulence and for the instrumental resolution, 49, 100, or 200 km s^{-1} , of the observed spectrum at the relevant phase to allow comparison. A range of different values of turbulence up to 800 km s^{-1} was tried when comparing the model and observed profiles and it was found that values below 500 km s^{-1} did not make a significant difference to the quality of the fits. Consequently, we adopted a uniform value of 500 km s^{-1} for the turbulence so that the influence of other parameters could more easily be seen. The resulting profile was added to the template underlying spectrum, being scaled to fit the observed profile.

We began by modelling the UIST observations (Table 1). The first three spectra in Fig. 11 bracket conjunction ($\phi = 0.9965$, O5 star in front and WCR facing us) and show a strong, single, subpeak. The next four spectra in Fig. 11 were all observed in 2008 December and show development of an asymmetric, rapidly broadening subpeak. Our initial models of the latter using the same parameters as for the RV variation ($\Delta\theta = 10^\circ$, downwind extent $3D$), recover the broadening but not the asymmetry, giving double peaks of equal height. The sequence ends close to quadrature ($\phi = 0.9965$), when any asymmetry between the leading and following

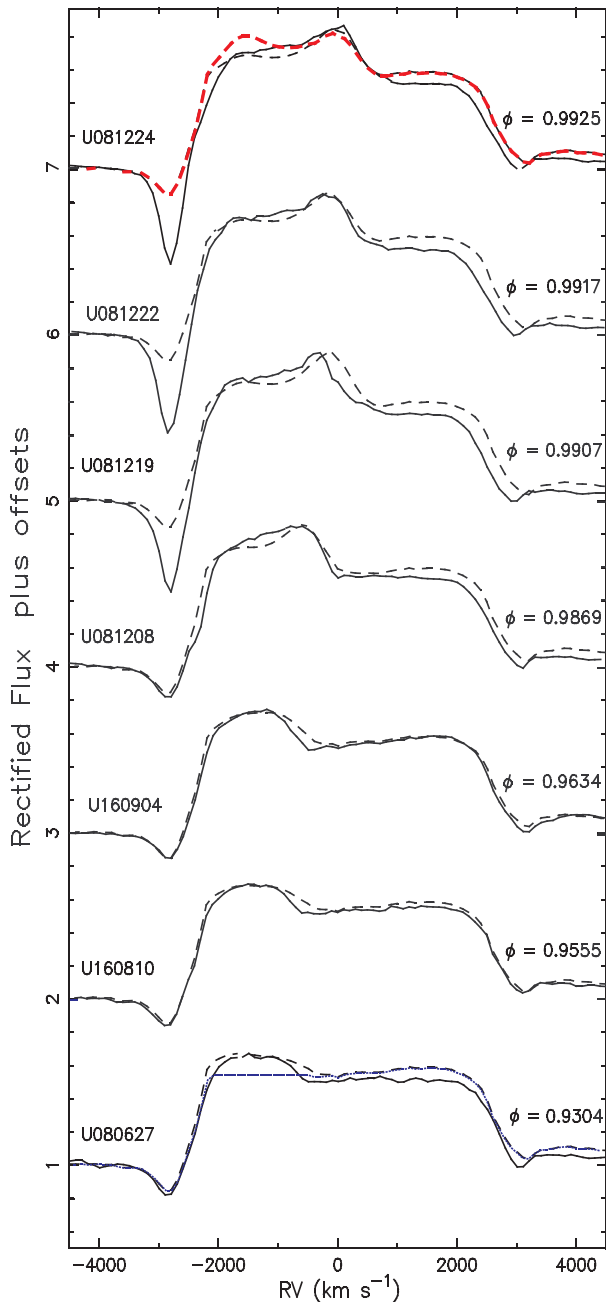


Figure 11. Seven profiles observed with UIST from phases 0.9301 (before conjunction) to 0.9923 (before quadrature) labelled with dates as UYYM-MDD, shifted for clarity, and compared with model profiles (broken lines) all calculated using $\Delta\theta = 10^\circ$, and a downstream distance of $3D$, as above, but also allowing for azimuthal asymmetry using coefficients $A_1 = A_2 = 0.5$. Overplotted (blue dotted line) on the earliest profile is the template spectrum without any subpeak emission. Another model for the 2008 December 24 (top) spectrum calculated without asymmetry to show the effect of the difference is shown in colour. The models were all convolved with Gaussian profiles for turbulence (500 km s^{-1}) and the instrument (200 or 100 km s^{-1} for the 2008 or 2016 observations, respectively).

arms of the WCR would be most readily observable in the profiles. We therefore examined this effect by running models having different values of the asymmetry parameters, A_1 and A_2 (equation 15), and found that $A_1 = A_2 = 0.5$, which has the effect of increasing the

emission from the leading arm at the expense of that in the following arm and out of the plane, gave reasonable matches to the 2008 December observations. The effect of this inclusion is illustrated for the December 24 spectrum, where models with and without the asymmetry are plotted. Inclusion of this asymmetry for all the models in Fig. 11 also provided ‘infill’ of the double peak of the earlier phase models through the redistribution of some WCR material into the plane.

A stronger manifestation of this asymmetry may be evident in the comparison of the observed and modelled *Chandra* High Energy Transmission Grating (HETG)–Medium Energy Grating (MEG) line profiles recently presented by Zhekov (2021, fig. 8). The observed profiles for ‘Obs 1’, corresponding to $\phi = 0.9863$, close to that of our U081208 spectrum (Fig. 11), generally show single peaks close to the red ends of the double-peak model profiles. This suggests that the region of the WCR where the Si XIV, Mg XII, and Ne X lines form shares the azimuthal asymmetry of that where the $1.083\text{-}\mu\text{m}$ subpeak forms, producing stronger emission from the leading arm. This needs to be investigated further using hydrodynamical models of the WCR and its emissivity (cf. Lamberts et al. 2012). The central velocities of the X-ray lines, -618 to -660 km s^{-1} (Pollock et al. 2005), are close to that (-690 km s^{-1}) of $1.083\text{-}\mu\text{m}$ peak but the X-ray profiles fall off more sharply to the blue.

Our next profile comes from the 2016 December 15 GNIRS observation (labelled G161215 in Fig. 12) at phase $\phi = 0.9987$, an interval of $1.006P_{\text{orb}}$ after the last of the 2008 UIST spectra. It is quite unlike the other profiles: either there is an additional broad emission peak centred near $\text{RV} = -1700 \text{ km s}^{-1}$, or the emission has become very broad and has developed a broad absorption centred near -1550 km s^{-1} . As noted above, the telluric correction for this observation had to be taken from a spectrum observed on a different night, but there is no way that the broad feature could arise from a mismatch of telluric lines. Unfortunately, there were no observations immediately before or after it, so we cannot trace how the features developed. A model profile (Fig. 12) calculated using the same parameters as for the earlier profiles, apart from omitting the azimuthal asymmetry, can match the broad emission, but not the -1700 km s^{-1} emission feature. Evidently, an additional emitting structure has come into existence within the WCR.

In the 7 d between this last spectrum and the first of the sequence beginning on 2016 December 22, WR 140 went through periastron passage. The last of the sequence, December 27, was observed only 2 d before conjunction. At this phase, with the O5 star beyond the WC7 star and the opening of the WCR directed away from us, the geometry leads us to expect the central RV of the subpeak to show the greatest difference from that during the $\phi = 0.9554$ conjunction (Fig. 11) when the WCR opening was directed towards us, but the widths of the subpeaks to be the same (cf. Moffat, Marchenko & Bartzakos 1996; Lührs 1997). This is evidently not the case: plotted on the December 27 observed profile (Fig. 12) is a model (colour plot) of the subpeak calculated using the same parameters as the earlier data. Although this recovered the central RV, it is significantly narrower than the observed subpeak.

We therefore set out to fit the spectrum allowing the opening angle, θ , and the flow velocities, characterized by an arbitrary multiple of the flow velocities for this phase calculated from the stellar wind velocities as in the previous modelling, to be free parameters, but retaining $\Delta\theta = 10^\circ$ and the downstream extent of $3D$ for the twisting. The fitted profile with parameters $\theta = 50^\circ$ and an arbitrary flow velocity multiple 1.3 is shown (black) in Fig. 12. Models using the same parameters give reasonable fits to the December 22–24 subpeak profiles (Fig. 12). Also shown (colour) on the December 22 profile

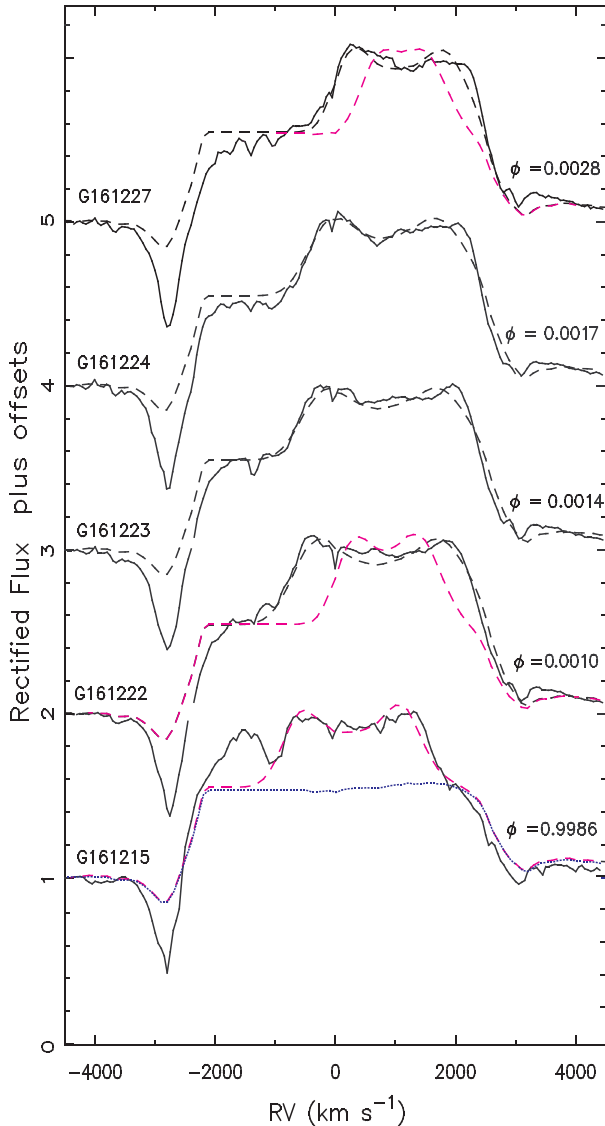


Figure 12. Profiles observed in 2016 December with GNIRS, with dates coded GYYMMDD, through periastron and close to conjunction compared with models (dashed lines, those in red using similar parameters to those adopted for modelling the earlier profiles, those in black the revised parameters derived for this phase range). Overplotted (blue dotted line) on the earliest profile is the template spectrum without any subpeak emission. The narrow absorption line near-zero RV is taken to arise in the O5 stellar photosphere.

is a model calculated using the ‘ $\theta = 34^\circ$ model’ parameters for comparison.

The wider θ could result either from a change in the shape of the WCR as a whole, as determined by the wind-momentum ratio η , or from a change in the region of the WCR where the $1.083\text{-}\mu\text{m}$ subpeak emission forms, i.e. in a shell offset from the CD by about 16° . The observation that the subpeak on the $5696\text{-}\text{\AA}$ C III line at the same phase in 2009 was *not* anomalously broad (Fahed et al. 2011), suggests that there was no significant change in the shape of the WCR, favours the latter alternative. We suggest that when the stars are closest, ionization of the helium by their radiation field restricts the formation of the He I emission in the inner regions of the WCR. It is not clear when this change came about; it is possible that the -1700 km s^{-1} flow observed in the December 15

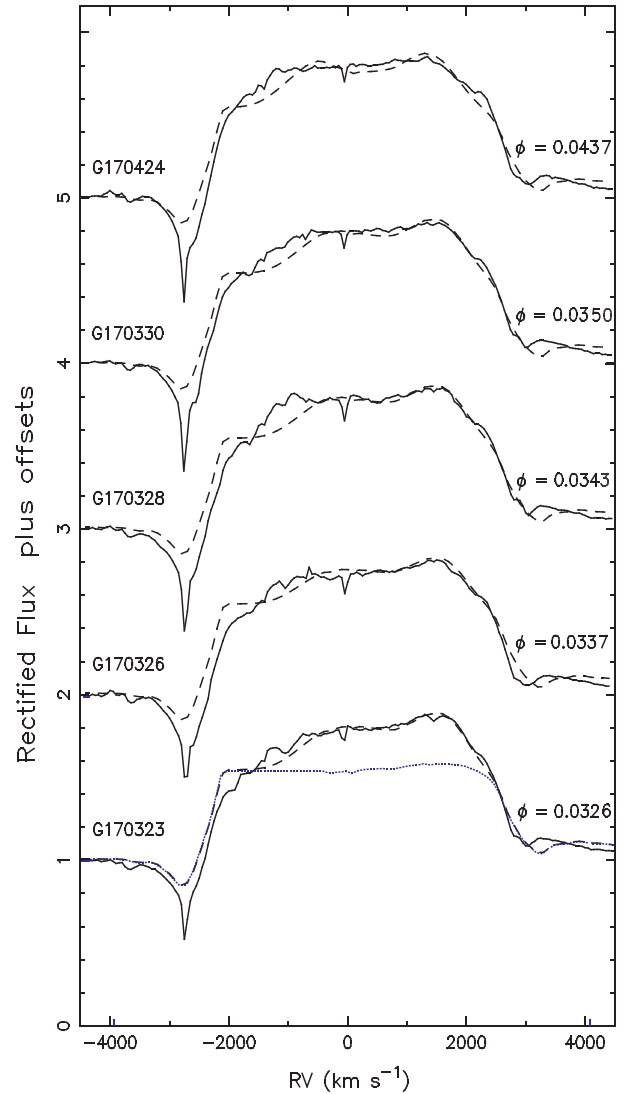


Figure 13. Profiles observed in 2017 March–April with GNIRS, with dates coded GYYMMDD, compared with models (dashed lines). Overplotted (blue dotted line) on the earliest profile is the template spectrum without any subpeak emission. The narrow absorption line near-zero RV is taken to arise in the O5 stellar photosphere.

spectrum was the beginning of the displaced plasma flow in the ‘following’ arm of the WCR judging from the sign of the RV. We also tested the possibility that the additional ionization could force the He I emission downstream in the WCR, which would show up in the profiles through requiring a greater downstream twisting length, but modelling did not support this possibility. We suggest that the enhanced flow velocity is also a consequence of the higher stellar radiation field in this phase range.

After the December sequence of observations, there was an interval of almost 3 months before the next sequence of spectra in 2017 March, followed by one in April, shown in Fig. 13. The last two spectra bracket orbital quadrature, when the WCR would have been viewed side-on and the RV amplitude greatest – accounting for the breadths of the subpeaks. The subpeak models shown use the same parameters as for the pre-periastron data with only the downstream distance for orbital twisting increased to $18D$, as derived above from the variation of central velocity with phase. Evidently, the anomalous

broadening of the December 22–27 spectra ascribed to an offset of the subpeak emission from the CD has ceased. The March–April sequence shows the gradual flattening of the subpeak profile as the emission fades. This continued in the final spectra observed in June, which show a weak, flat emission and are not modelled because they are not very different from the template profile devised above.

4 COMPARISON WITH OBSERVATIONS AT OTHER WAVELENGTHS

The absorption component of the 1.083- μm profile is the superimposition of those formed in the sightlines to the WC7 and O5 stars. Because the sightline to the WC7 star always passes through at least part of its own wind closest to the star, where the density is highest, we assume that component of the observed absorption to be constant and assign all of the variation observed to varying absorption along the sightline to the O5 star. After $\phi = 0.986$, when the sightline to the O5 star starts passing through the shocked WC7 wind in the WCR, we observe strong and variable absorption, which reaches a maximum shortly after periastron passage.

The X-ray absorption (Pollock et al., in preparation) also reaches a maximum at conjunction, just after periastron, when the WCR and X-ray source are beyond the WC7 star and suffer the greatest absorption. We have already drawn attention (Section 3.3 above) to a similarity in the forms of the increase towards maximum of the X-ray hardness ratio in the *RXTE* PCA data, a proxy for absorption, and the 1.083- μm profile absorption: both showing a pause near $\phi \simeq 0.995$.

Variations in the WCR also appear to be responsible for rapid changes seen in the ultraviolet spectrum. The sequence of the *International Ultraviolet Explorer* (*IUE*) spectra covering almost a whole orbit, including the 1993 periastron passage, observed by Setia Gunawan et al. (2001) show sudden strengthening and broadening of the C II, Si IV, and C IV resonance lines between phases 0.96 and 0.012 (on their elements; the phases on those used here are very similar). The deep absorption trough of the Si IV $\lambda\lambda 1394, 1493$ Å doublet became saturated and broadened from 400 to 1200 km s⁻¹, then extending from -3200 to -2000 km s⁻¹, while that of the C IV $\lambda\lambda 1548, 1551$ Å doublet behaved similarly. Both profiles took a long time for the troughs to recover their ‘quiescent’, pre-periastron breadths – until phases 0.3 and 0.6, respectively. If these effects arise in the sightline to the O5 star through the WCR, which seems probable,⁶ they demonstrate that the WCR takes a long time to recover from the periastron passage.

The He I 1.083- μm subpeak emission shows a very similar effect, varying smoothly before periastron and very irregularly after it. The subpeak fluxes were significantly greater than those before periastron at the same stellar separations (e.g. at $\phi = 0.965$ and 0.035), when the pre-shock wind densities and hence material available to the WCR, would have been the same.

The asymmetry about periastron of the intrinsic non-thermal radio emission may be related. White & Becker (1995) observed WR 140 around its orbit at 2, 6, and 20 cm and were thus able to derive the variation of both the intrinsic non-thermal emission and the circumstellar free-free absorption with phase. The intrinsic 2-cm non-thermal emission varied from ~ 2 mJy near periastron, reaching

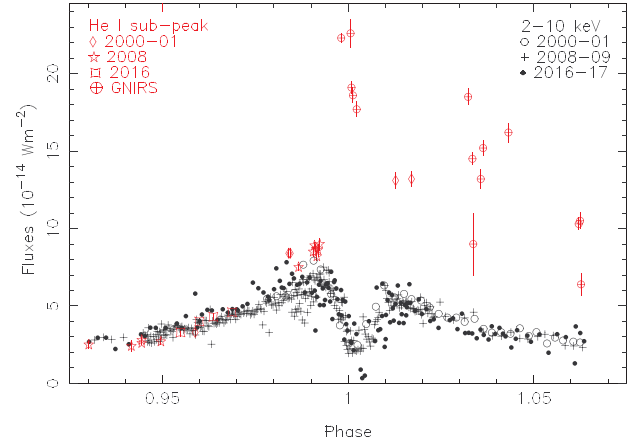


Figure 14. Comparison of the absorption-corrected 2–10-keV X-ray and 1.083- μm subpeak fluxes (colour) plotted against phase.

a maximum at $\phi \sim 0.7$; the flux density at $\phi \simeq 0.8$ was three times that at $\phi \simeq 0.2$. The authors suggested a model in which the wind of WR 140 was flattened into a disc, but this was not supported by spectropolarimetry (Harries, Hillier & Howarth 1998), which showed no line effect – so the mechanism for the variation of the intrinsic non-thermal emission remains an open question.

Another manifestation of asymmetric behaviour about periastron can be seen in the optical photometry: the *UBV* magnitudes in 2001 after periastron ($\phi = 0.020$ – 0.055) show dips attributed to formation of clumps of dust in the line of sight (Marchenko et al. 2003), whereas the photometry before periastron did not show this phenomenon. This could be related to the clumps in the WCR after periastron suggested as the cause of the strength and variation of the 1.083- μm subpeak emission in the same phase range rather than to the substantial dust clouds formed each periastron passage. Although their strong IR ‘excess’ emission is observed only after periastron, this does not indicate any asymmetry about periastron of the wind-collision process, but reflects the prolonged cooling of the newly formed dust as it moves away from the stars (Williams et al. 1990, 2009).

The flux (Tables 1 and 2) in the subpeak on the He I profile is a significant source of cooling for the shock-heated material, reaching a maximum of $2.3(\pm 0.1) \times 10^{-13} \text{ W m}^{-2}$ at periastron. At maximum, the subpeak on the 5696-Å C III line had an EW of 10.9 km s⁻¹ (Fahed et al. 2011), which can be converted to an integrated flux of $1.9 \times 10^{-14} \text{ W m}^{-2}$, corrected for interstellar reddening. Other lines in the visible also show subpeak emission (e.g. 5876-Å He I). In the phase range $\phi = 0.93$ – 0.97 , the subpeak flux was very similar to the absorption-corrected 2–10-keV X-ray flux (Fig. 14), increasing as D^{-1} and was an approximately equal contributor to the cooling of the shock. The subpeak flux continued increasing at this rate until $\phi \sim 0.99$ (Section 3.5 above), after which it increased more quickly while the X-ray flux fell below the D^{-1} dependence and went through a minimum close to conjunction, as discussed by Pollock et al. (in preparation). After periastron, the X-ray flux recovered its earlier D^{-1} dependence near $\phi = 0.02$, whereas the 1.083- μm subpeak emission remained strong and very variable.

5 CONCLUSIONS

New observations of the He I 1.083- μm line around the times of the 2008 and 2016 periastron passages showed a strong and variable

⁶Both profiles also show broad absorption extending to +3400 and +2000 km s⁻¹, which may have formed in the pre-collision WC7 wind as the system was close to conjunction with the WCR beyond the WC7 star at this phase.

P Cygni profile. Both emission and absorption components of the profile are powerful diagnostics, of very different scope. The emission comes from the system as a whole, both stars and WCR, whereas the absorption samples a tiny part of the system along two pencil beams, whose varying positions are well known from the orbit. The strength of the absorption component showed a sharp increase at $\phi = 0.986$ as the ‘following’ arm of the WCR crossed our sightline to the O5 star, allowing us to set a tight limit on the opening half-opening angle of the CD in the WCR: $\theta = 34^\circ \pm 1^\circ$.

Particularly near and after periastron, when our sightline to the O5 component crossed the WCR, the strength and breadth of the absorption component varied on a short time-scale, suggesting turbulence and instabilities in the WCR, as expected theoretically (e.g. Stevens et al. 1992; Walder & Folini 2003). The central velocity of the absorption, however, was not consistent with the expected velocity field in the WCR while relation to the wind of the WC7 star was also problematic. This remains a conundrum to be resolved.

An emission subpeak was visible on top of the normally flat-topped emission profile from our earliest observation at phase 0.93. Until phase ~ 0.99 , its flux was approximately proportional to the inverse of the stellar separation, D , as expected from an adiabatic post-shock wind. Between phases 0.99 and 0.01, the variation with separation was steeper, nearer to being proportional to D^{-2} , suggesting increased cooling of the shocked wind, consistent with the condensation of dust (which requires efficient cooling) in this short interval. Thereafter, the fading of the subpeak emission was very irregular but it was always significantly stronger than that at the corresponding stellar separations before periastron. As the amounts of stellar wind material available for compression in the WCR, which depend on stellar separation through the undisturbed wind densities, would have been the same, we suggest that the extra, variable emission was caused by the formation of clumps in the shock-compressed wind. Our early observations found the subpeak flux to be approximately equal to the X-ray flux but, after $\phi \simeq 0.97$, the subpeak flux exceeded the X-ray flux and became the major source of cooling of the shock.

New geometric models for the profiles of the subpeaks have been developed. They allow for emission from the region of the WCR extending $\Delta\theta$ on the WC7 wind side of the CD, which corresponds to a region on the CD where the shock-compressed wind is still accelerating from the shock apex to its asymptotic value downstream where the WCR can be approximated by a cone. Consequently, the flow has a range of velocities and angles to the axis of symmetry. The models also allow for the twisting of the flow downstream caused by orbital motion and for the occurrence of the wind collision so close to the O5 star that its wind could not have achieved its terminal velocity if it accelerated according to a β -law. Both these effects vary around the orbit. It was possible to recover the variation of the flux-weighted RV of the subpeak emission over the phase range 0.93–1.06 that, because of the high eccentricity of the orbit, includes both the conjunctions and both the quadratures thereby sampling practically the whole orbital geometry, with a model based on the occultation-determined opening angle $\theta = 34^\circ$, and flow velocities calculated from the stellar wind velocities following Cantó et al. (1996). Adjustable parameters were the flow thickness, $\Delta\theta$, and the downstream extent over which emission from the twisted compressed wind needed to be taken into account, expressed as a multiple of the stellar separation, D . We found all the data could be fit with $\Delta\theta = 10^\circ$. Prior to phase ~ 0.01 , twisting of the WCR for $3D$ downstream was indicated; subsequently, in the latter phase range in which the fluxes suggested the post-shocked wind was heavily clumped, modelling the effect of WCR twisting required an extent

of $18D$, suggesting survival of the clumps a significant distance downstream.

Fitting the observed profiles revealed different regimes in three different phase ranges. Up to $\phi = 0.9925$, the profiles could be fit using the same parameters as for the phase dependence of the RV with one refinement: allowance was made for azimuthal asymmetry of the emission about the WCR axis, favouring the ‘leading’ arm of the WCR. This may also explain the difference between published observed and modelled profiles of X-ray lines observed with *Chandra* in this phase range. Certainly, the comparison of profiles of the subpeak and X-ray lines observed contemporaneously can be expected to yield fresh insights to the WCR phenomenon. Closer to periastron, modelling showed that the subpeak emission came from a region characterized by a larger opening angle, suggesting formation in a shell offset from the CD, possibly because of ionization of the helium by the intense stellar radiation field. Subsequently, from $\phi \simeq 0.03$, the profiles could again be fitted by the parameters used for the pre-periastron data, suggesting that the WCR and location of the subpeak emission had recovered from the disruption of periastron passage. These profiles did not suggest greater subpeak emission in the leading arm of the WCR, perhaps because it was moving into less dense regions of the stellar winds.

These geometric models take no account of the variation in subpeak emissivity in the WCR and its variation around the orbit, all which need to be modelled to exploit the power of the $1.083\text{-}\mu\text{m}$ profile as a diagnostic of the WCR.

Further observations of the profile are also called for earlier in phase than our first observation to track the reduction in absorption to map the leading arm of the WCR, to time appearance of the subpeak, and to get a better template spectrum for defining the subpeak emission when it is weak, and, particularly, around periastron to track the rapid changes shown by our patchy coverage, such as the dependence of the flux on stellar separation, D , the development of the -1700 km s^{-1} feature at $\phi = 0.9987$ (if it recurs periodically), and the subsequent broadening of the subpeak in the approach to conjunction. The $1.083\text{-}\mu\text{m}$ He I profile has proved to be a powerful diagnostic of the colliding winds in WR 140 and has the potential to reveal much more.

ACKNOWLEDGEMENTS

We would like to thank UKIRT and Gemini Service Observing astronomers for obtaining the spectra for this study. Prior to 2014 November, UKIRT was operated by the Joint Astronomy Centre, Hilo, Hawaii, on behalf of the U.K. Science and Technology Facilities Council. When the 2016 observations were acquired, UKIRT was supported by NASA and operated under an agreement among the University of Hawaii, the University of Arizona, and Lockheed Martin Advanced Technology Center; operations were enabled through the cooperation of the East Asian Observatory. This study also based on observations obtained at the international Gemini Observatory, a program of NSF’s NOIRLab, which is managed by the Association of Universities for Research in Astronomy (AURA) under a cooperative agreement with the National Science Foundation, on behalf of the Gemini Observatory partnership: the National Science Foundation (USA), National Research Council (Canada), Agencia Nacional de Investigación y Desarrollo (Chile), Ministerio de Ciencia, Tecnología e Innovación (Argentina), Ministério da Ciência, Tecnologia, Inovações e Comunicações (Brazil), and Korea Astronomy and Space Science Institute (Republic of Korea). It is a pleasure to thank Ken Gayley for a helpful referee’s report. AFJM is grateful to NSERC (Canada) for financial aid. PMW is grateful to

the Institute for Astronomy, University of Edinburgh, for continued hospitality and access to the facilities of the Royal Observatory Edinburgh.

DATA AVAILABILITY

The data underlying this paper are available at the Canadian Astronomy Data Centre (<https://www.cadc-ccda.hia-ihc.nrc-cnrc.gc.ca/en/>) or will be shared on reasonable request to the corresponding author.

REFERENCES

- Cantó J., Raga A. C., Wilkin F. P., 1996, *ApJ*, 469, 729
- Conti P. S., Howarth I. D., 1999, *MNRAS*, 302, 145
- Dessart L., Crowther P. A., Hillier D. J., Willis A. J., Morris P. W., van der Hucht K. A., 2000, *MNRAS*, 315, 407
- Eenens P. R. J., Williams P. M., 1994, *MNRAS*, 269, 1082
- Eenens P. R. J., Williams P. M., Wade R., 1991, *MNRAS*, 252, 300
- Eichler D., Usov V., 1993, *ApJ*, 402, 271
- Elias J. H., Joyce R. R., Liang M., Muller G. P., Hileman E. A., George J. R., 2006, in McLean I. S., Masanori I., eds, *Proc. SPIE Vol. 6269, Ground-Based and Airborne Instrumentation for Astronomy*. SPIE, Bellingham, p. 62694C
- Fahed R. et al., 2011, *MNRAS*, 418, 2
- Gayley K. G., 2009, *ApJ*, 703, 89
- Girard T., Willson L. A., 1987, *A&A*, 183, 247
- Harries T. J., Hillier D. J., Howarth I. D., 1998, *MNRAS*, 296, 1072
- Hervieux Y., 1995, in van der Hucht K. A., Williams P. M., eds, *Proc. IAU Symp. 163, Wolf-Rayet Stars: Binaries; Colliding Winds; Evolution*. Kluwer, Dordrecht, p. 460
- Hill G. M., Moffat A. F. J., St-Louis N., 2002, *MNRAS*, 335, 1069
- Hill G. M., Moffat A. F. J., St-Louis N., 2018, *MNRAS*, 474, 2987
- Hillier D. J., 1989, *ApJ*, 347, 392
- Ignace R., Bessey R., Price C. S., 2009, *MNRAS*, 395, 962
- Kobulnicky H. A. et al., 2012, *ApJ*, 756, 50
- Lamberts A., Dubus G., Lesur G., Fromang S., 2012, *A&A*, 546, A60
- Lühns S., 1997, *PASP*, 109, 504
- Marchenko S. V. et al., 2003, *ApJ*, 596, 1295
- Moffat A. F. J., Marchenko S. V., Bartzakos P., 1996, *Rev. Mex. Astron. Astrofis. Conf. Ser.*, 5, 38
- Monnier J. D. et al., 2011, *ApJ*, 742, L1
- Nazé Y., Mahy L., Damerdji Y., Kobulnicky H. A., Pittard J. M., Parkin E. R., Absil O., Blomme R., 2012, *A&A*, 546, A37
- Parkin E. R., Pittard J. M., 2008, *MNRAS*, 388, 1047
- Pittard J. M., Dawson B., 2018, *MNRAS*, 477, 5640
- Pollock A. M. T., Corcoran M. F., Stevens I. R., Williams P. M., 2005, *ApJ*, 629, 482
- Ramsay Howat S. K. et al., 2004, in Moorwood A. F. M., Masanori I., eds, *Proc. SPIE Vol. 5492, Ground-Based Instrumentation for Astronomy*. SPIE, Bellingham, p. 1160
- Repolust T., Puls J., Herrero A., 2004, *A&A*, 415, 349
- Sander A., Shenar T., Hainich R., Gímez-García A., Todt H., Hamann W. R., 2015, *A&A*, 577, A13
- Setia Gunawan D. Y. A., van der Hucht K. A., Williams P. M., Henrichs H. F., Kaper L., Stickland D. J., Wamsteker W., 2001, *A&A*, 376, 460
- Stevens I. R., Howarth I. D., 1999, *MNRAS*, 302, 549
- Stevens I. R., Blondin J. M., Pollock A. M. T., 1992, *ApJ*, 386, 265
- Sugawara Y. et al., 2015, *PASJ*, 67, 121
- Taranova O. G., Shenavrin V. I., 2011, *Astron. Lett.*, 37, 30
- Thomas J. D. et al., 2021, preprint ([arXiv:2101.10563](https://arxiv.org/abs/2101.10563))
- Tuthill P. G., Monnier J. D., Lawrance N., Danchi W. C., Owocki S. P., Gayley K. G., 2008, *ApJ*, 675, 698
- Usov V. V., 1991, *MNRAS*, 252, 49
- Varricatt W. P., Williams P. M., Ashok N. M., 2004, *MNRAS*, 351, 1307
- Vreux J.-M., Andriat Y., Biemont E., 1990, *A&A*, 238, 207
- Walder R., Folini D., 2003, in van der Hucht K., Herrero A., Esteban C., eds, *Proc. IAU Symp. 212, A Massive Star Odyssey: From Main Sequence to Supernova*. Astron. Soc. Pac., San Francisco, p. 139
- White R. L., Becker R. H., 1995, *ApJ*, 451, 352
- Williams P. M., 1999, in Wolf B., Stahl O., Fullerton A. W., eds, *Lecture Notes in Physics Vol. 523, Proc. IAU Colloq. 169, Variable and Non-Spherical Stellar Winds in Luminous Hot Stars*. Springer-Verlag, Berlin, p. 275
- Williams P. M., Eenens P. R. J., 1989, *MNRAS*, 240, 445
- Williams P. M., van der Hucht K. A., Pollock A. M. T., Florkowski D. R., van der Woerd H., Wamsteker W. M., 1990, *MNRAS*, 243, 662
- Williams P. M., van der Hucht K. A., Bouchet P., Spoelstra T. A. T., Eenens P. R. J., Geballe T. R., Kidger M. R., Churchwell E., 1992, *MNRAS*, 258, 461
- Williams P. M. et al., 2009, *MNRAS*, 395, 1749
- Williams P., Varricatt W., Adamson A., 2013, in Adamson A., Davies J., Robson I., Robson I., eds, *Astrophysics and Space Science Proceedings Vol. 37, Thirty Years of Astronomical Discovery with UKIRT*. Springer, Dordrecht, p. 151
- Zhekov S. A., 2021, *MNRAS*, 500, 4837

This paper has been typeset from a \LaTeX file prepared by the author.